Available online at www.sciencedirect.com
ScienceDirect
Journal of Computational Physics 227 (2008) 4207–4243
JOURNAL OF COMPUTATIONAL PHYSICS
www.elsevier.com/locate/jcp

Numerical simulation of viscoelastic flows using integral constitutive equations: A finite difference approach

M.F. Tomé [a,*], M.S.B. de Araujo [a], M.A. Alves [b], F.T. Pinho [c,d]

[a] *Departamento de Matemática Aplicada e Estatística, ICMC/USP—Instituto de Ciências Matemáticas e de Computação, Caixa Postal 668, 13560-970, São Carlos, SP, Brazil*
[b] *Departamento de Engenharia Química, CEFT, Faculdade de Engenharia da Universidade do Porto, Rua Dr. Roberto Frias s/n, 4200-465 Porto, Portugal*
[c] *CEFT, Faculdade de Engenharia da Universidade do Porto, Rua Dr. Roberto Frias s/n, 4200-465 Porto, Portugal*
[d] *Universidade do Minho, Largo do Paço, 4704-553 Braga, Portugal*

Received 5 March 2007; received in revised form 6 December 2007; accepted 21 December 2007
Available online 9 January 2008

Abstract

This work presents a numerical technique for simulating incompressible, isothermal, viscoelastic flows of fluids governed by the upper-convected Maxwell (UCM) and K–BKZ (Kaye–Bernstein, Kearsley and Zapas) integral models. The numerical technique described herein is an extension of the GENSMAC method to the solution of the momentum and mass conservation equations to include integral constitutive equations. The governing equations are solved by the finite difference method on a staggered grid using a Marker-and-Cell approach. The Finger tensor $\mathbf{B}_{t'}(t)$ is computed in an Eulerian framework using the ideas of the *deformation fields* method. However, improvements to the *deformation fields* method are introduced: the Finger tensor $\mathbf{B}_{t'}(\mathbf{x},t)$ is obtained by a second-order accurate method and the stress tensor $\tau(\mathbf{x},t)$ is computed by a second-order quadrature formula. The numerical method presented in this work is validated by comparing the predictions of velocity and stress fields in two-dimensional fully-developed channel flow of a Maxwell fluid with the corresponding analytic solutions. Furthermore, the flow through a planar 4:1 contraction is investigated and the numerical results were compared with the corresponding experimental data. Finally, the UCM and the K–BKZ models were used to simulate the planar 4:1 contraction flow over a wide range of Reynolds and Weissenberg numbers and the numerical results obtained are in agreement with published data.

Keywords: Integral constitutive equation; Upper-convected Maxwell model; K–BKZ model; Deformation fields method; Finite difference; Viscoelastic flow

1. Introduction

The numerical simulation of incompressible and compressible non-Newtonian fluid flows is an active area of research in computational mechanics, but most numerical techniques for simulating viscoelastic fluid flows

* Corresponding author.
E-mail address: murilo@icmc.usp.br (M.F. Tomé).

0021-9991/$ - see front matter © 2007 Elsevier Inc. All rights reserved.
doi:10.1016/j.jcp.2007.12.023

employ differential rather than integral constitutive models. If many rheological constitutive equations have both a differential and an integral form, other models exist only in one form or become extremely complex when transforming from one form to another without simplifying assumptions. Therefore, efficient numerical methods are required to deal with both types of equations. When dealing with differential constitutive equations only present and recent fields of velocity and stress are required to the computation of the stress tensor, whereas for integral models the calculation of the stress field needs an extensive account of the history of past deformations. Hence, integral models require the use of time-dependent numerical methods, even when the flow is steady, leading to a large overhead of computational resources. Therefore, it comes as no surprise that the majority of numerical investigations relies on differential constitutive equations, using diverse numerical methods such as finite elements (e.g. [23,27,28,7], to cite only a few), finite volumes (e.g. [26,52]) and finite difference (e.g. [45,48]). A more extensive review of computational rheology up to 2003 is presented in the book by Owens and Phillips [32]. Essentially only over the last decade integral models have been used more frequently.

Numerical methods for solving integral viscoelastic models have usually employed finite elements (e.g. [29,34,19,31]) and one of the most used integral constitutive equations is the K–BKZ model [17,5], which provides a good fitting to experimental data for some fluids and therefore, it has been studied by various investigators (e.g. [19,21,20,22,42]). The KBK–Z model is a integral equation containing the information about the deformation history of the fluid, and this particularity is enough to bring numerical challenges, which have been investigated by a number of researchers in the literature (e.g. [43,44,41,40]). An updated review on finite element techniques for solving complex flows of fluids described by integral constitutive models has been presented by Keunings [18]. This review concluded that both the Lagrangian integral method [14] and the deformation fields method [34] can cope with transient flows.

The numerical simulation of the flow through a planar contraction is a classical benchmark problem in computational rheology. Contraction flows are interesting because non-Newtonian fluids exhibit a wide variety of behaviours depending on their rheology. In particular, the study of the mechanisms involved in the formation of corner and lip vortices has attracted the attention of many researchers. It has been shown that the length and intensity of these vortices change with the Weissenberg and Reynolds numbers as well as with the type of the contraction (planar or axisymmetric; with a sharp or rounded entry, etc.) and the fluid rheology. There are several numerical works devoted to the simulation of contraction flows and the results presented depend on the methodology and the constitutive equation employed. On the experimental side there is also a significant number of works. For instance, Evans and Walters [9] analysed the effect of small changes in the geometry of the contraction entrance. They did a series of experiments using Boger fluids and shear-thinning fluids and showed that the growth of the vortices was a function of the contraction ratio. White and Baird [51] investigated the behaviour of polystyrene (PS) and low density polyethylene (LDPE) in planar 4:1 contraction and reported that for the PS fluid no secondary flow was formed, although the shear viscosity of both fluids was similar. It was suggested that the formation of vortices depended on extensional properties of the fluid and in particular, the extensional stress growth. Purnode and Crochet [36] employed the FENE-P model to simulate the experimental results of Evans and Walters [9,10] for the flow through a planar contraction. They investigated the influence of the contraction ratio, the concentration of the polymer and the shape of the corners at the contraction entrance. The numerical results presented good qualitative agreement with the experimental results showing the appearance of "lip vortices" at several Weissenberg and Reynolds numbers. Mompean and Deville [26] used an algorithm based on the MAC method [13] with finite volumes for simulating the two-dimensional flow of an Oldroyd-B fluid in a 4:1 planar contraction. The three-dimensional flow through a 4:1 contraction was also investigated by Xue et al. [53] using the UCM and the PTT constitutive equations. Their results showed that experimental measurements can be reproduced if the fluid is characterized by an appropriate constitutive equation. Mesh refinement for the 2D case using an Oldroyd-B model was also considered in the work of Xue et al. [53]. They reported that different results related to vortex activity were obtained depending on the degree of refinement of the mesh used in the calculations. Alves et al. [3] studied experimentally the flow of Boger fluids in a 4:1 3D square/square contraction, and observed complex flow patterns with appearance of a lip vortex followed by divergent streamlines and elastic instabilities at higher flow rates.

Contraction flows have also been simulated by integral models. Viriyayuthakorn and Caswell [50] presented a finite element technique for solving a single memory integral equation. They calculated the integral by a

Laguerre quadrature formula and presented a technique for computing the particle paths. They simulated the flow through a 4:1 axisymmetric contraction and the results showed an enhancement of the size of the corner vortex when the Deborah/Weissenberg number increased from one to two. Luo and Mitsoulis [21] presented a finite element technique for simulating axisymmetric contraction flows using the K–BKZ constitutive equation. They performed a study of the effect of the extensional viscosity on the behaviour of the vortices. They showed that by varying the parameter β in the K–BKZ equation the size of the corner vortex changed and the appearance of lip vortices was affected. Later, Luo [19] presented a numerical technique using finite volumes and an ADI method for solving the momentum equations on a staggered grid. Numerical results of the flow through a 5.75:1 contraction using the K–BKZ equation were presented and reported a better performance than the finite element method used in the previous work [21].

In this work, we develop a finite difference technique for simulating flows governed by integral constitutive equations and in particular we solve the upper-convected Maxwell (UCM) and the K–BKZ constitutive equations. The conservation equations are solved following the approach used by Tomé et al. [45]. To calculate the extra-stress tensor we employ the deformation fields method introduced by Peters et al. [34] (see also [49]). This methodology allows the Finger tensor to be calculated in a fixed frame of reference. Peters et al. [34] used the fact that the upper-convected derivative of the Finger tensor is null in order to convect it in time. Later, Hulsen et al. [15] showed the numerical drawbacks of this approach and proposed a modification by adding to the upper-convected derivative a term containing a derivative with respect to the elapsed time, $s = t - t'$. In this work, the Finger tensor is calculated at each time-step with the equation used by Peters et al. [34], but employing a different approach from both works [15,34].

This paper is organized as follows: after presenting the governing equations in Section 2, the methodology employed for calculating the extra-stress tensor is described in Section 3. The numerical method is outlined in Section 4 and the finite difference approximations are described in Section 5. Section 6 is used to validate the procedure to calculate the extra-stress in simple shear and elongational flows. Section 7 presents numerical results for the flow of UCM and K–BKZ fluids in a two-dimensional channel and includes a mesh refinement study to quantify their numerical uncertainty. In Section 7.3, the 4:1 planar contraction flow measured by Quinzani et al. [37] is simulated using the K–BKZ constitutive equation and the predictions are compared with their experimental data. Finally, a parametric investigation of the same flow is carried out for UCM and K–BKZ fluids in order to assess the effect of Weissenberg number and some of the results are compared with data of Alves et al. [1] as well as with new results using the same finite-volume code [1,2] written for the differential form of the UCM constitutive equation. A summary and conclusions close the paper.

2. Basic equations

The governing equations for isothermal incompressible flows are the mass and the momentum conservation equations, given by

$$\nabla \cdot \mathbf{v} = 0, \tag{1}$$

$$\rho_0 \left[\frac{\partial \mathbf{v}}{\partial t} + \nabla \cdot (\mathbf{v}\mathbf{v}) \right] = -\nabla p + \eta_0 \nabla^2 \mathbf{v} + \nabla \cdot \mathbf{S} + \rho_0 \mathbf{g}, \tag{2}$$

where ρ_0 is the fluid density, $\mathbf{v}$ is the velocity vector, p is the pressure, $\mathbf{g}$ is the acceleration of gravity vector and $\mathbf{S}$ is an elastic tensor related to the extra-stress tensor of the fluid by $\boldsymbol{\tau} = \eta_0 \dot{\boldsymbol{\gamma}} + \mathbf{S}$ where $\dot{\boldsymbol{\gamma}} = \nabla \mathbf{v} + (\nabla \mathbf{v})^{\mathrm{T}}$ is the rate of deformation tensor. This decoupling of the extra-stress tensor into Newtonian and elastic contributions is inspired by the EVSS method of Rajagopalan et al. [39] for differential constitutive equations and promotes numerical stability.

The extra-stress tensor is given by an adequate constitutive equation, such as the integral K–BKZ constitutive equation presented by Papanastasiou et al. [33]

$$\boldsymbol{\tau}(t) = \int_{-\infty}^{t} M(t - t') H(I_1, I_2) \mathbf{B}_{t'}(t) \mathrm{d}t', \tag{3}$$

where the memory function

$$M(t-t') = \sum_{m=1}^{m_1} \frac{a_m}{\lambda_m} \mathrm{e}^{-\frac{t-t'}{\lambda_m}} \tag{4}$$

contains a spectrum of relaxation times and viscosity coefficients. The function $H(I_1, I_2)$ is given by

$$H(I_1, I_2) = \frac{\alpha}{\alpha + \beta I_1 + (1-\beta) I_2}.$$

The tensor $\mathbf{B}_{t'}(t)$ is the Finger tensor, which quantifies the deformation, i.e. the position of fluid particles at present time t relative to their position at the elapsed time t'. Other quantities appearing in (3) are $I_1 = \mathrm{tr}[\mathbf{B}_{t'}(t)]$ and $I_2 = \frac{1}{2}((I_1)^2 - \mathrm{tr}[\mathbf{B}^2_{t'}(t)])$, the first and second invariants of $\mathbf{B}_{t'}(t)$, respectively. The parameters a_m, λ_m, α and β of the model are obtained from the rheological fluid properties.

We shall also be interested in the upper-convected Maxwell (UCM) model given in its integral form as

$$\boldsymbol{\tau}(t) = \int_{-\infty}^{t} M(t-t') \mathbf{B}_{t'}(t) \mathrm{d}t'. \tag{5}$$

This model is a particular case of the K–BKZ equation and is obtained by setting $H(I_1, I_2) = 1$. Although the UCM model is less realistic it is frequently used in numerical investigations due to its simplicity and especially the numerical problems it poses due to unbounded stresses that may develop in extensional flows. Indeed, as is well-known, robust methods developed for the UCM model will work well with other more realistic constitutive equations.

Eqs. (1)–(5) can be written in non-dimensional form by using the following dimensionless variables:

$$\bar{\mathbf{v}} = \frac{\mathbf{v}}{U}, \quad \bar{\mathbf{x}} = \frac{\mathbf{x}}{L}, \quad \bar{t} = \frac{U}{L} t, \quad \bar{\mathbf{g}} = \frac{\mathbf{g}}{g}, \quad \bar{p} = \frac{p}{\rho_0 U^2}, \quad \overline{\mathbf{S}} = \frac{\mathbf{S}}{\rho_0 U^2},$$

$$\bar{\eta} = \frac{\eta}{\eta_0}, \quad \bar{\rho} = \frac{\rho}{\rho_0}, \quad \bar{\lambda}_m = \frac{\lambda_m}{\lambda_0}, \quad \bar{a}_m = \frac{a_m}{\rho_0 U^2} \quad (m = 1, 2, \ldots, m_1),$$

where $L, U, g, \eta_0, \rho_0, \lambda_0$ are characteristic values for length, velocity, gravity, viscosity, density and relaxation time, respectively. Introducing these variables in Eqs. (1)–(3) leads to the following set of normalised equations, which must be solved numerically:

$$\nabla \cdot \mathbf{v} = 0, \tag{6}$$

$$\frac{\partial \mathbf{v}}{\partial t} + \nabla \cdot (\mathbf{v}\mathbf{v}) = -\nabla p + \frac{1}{Re} \nabla^2 \mathbf{v} + \nabla \cdot \mathbf{S} + \frac{1}{Fr^2} \mathbf{g}, \tag{7}$$

$$\boldsymbol{\tau}(t) = \int_{-\infty}^{t} \sum_{m=1}^{m_1} \frac{a_m}{\lambda_m We} \mathrm{e}^{-\frac{t-t'}{\lambda_m We}} \mathbf{f}[\mathbf{B}_{t'}(t)] \mathrm{d}t', \tag{8}$$

$$\mathbf{S} = \boldsymbol{\tau} - \frac{1}{Re} \dot{\boldsymbol{\gamma}}, \tag{9}$$

where $\mathbf{f}[\mathbf{B}_{t'}(t)] = H(I_1, I_2)\mathbf{B}_{t'}(t)$ for the K–BKZ model and $\mathbf{f}[\mathbf{B}_{t'}(t)] = \mathbf{B}_{t'}(t)$ if the UCM model is employed. The bars were omitted for clarity. In these equations, $Re = \frac{\rho_0 UL}{\eta_0}$ is the Reynolds number and $We = \lambda_0 \frac{U}{L}$ is the Weissenberg number.

2.1. Boundary conditions

In order to solve Eqs. (6)–(9) it is necessary to specify boundary conditions. For the velocity vector these are: on rigid boundaries the no-slip condition, at fluid entrances (inflows), usually far from the region of interest where the flow is assumed fully-developed, the normal velocity (U^{n}) is specified by a parabolic profile and the tangential velocity (U^{t}) is set to zero. The indices n, and t denote normal and tangential directions relative to the boundary, respectively. At fluid exits (outflows), again located far from the region of interest, the flow is assumed fully-developed and so the homogeneous Neumann condition $\frac{\partial \mathbf{u}}{\partial \mathrm{n}} = 0$ is adopted.

The calculation of the extra-stress tensor is discussed in the next section.

3. Computation of the extra-stress tensor

The variable used by Peters et al. [34] and Hulsen et al. [15], to perform the integration of (8) to calculate the extra-stress is the elapsed time, $s = t - t'$, i.e.

$$\boldsymbol{\tau}(t) = \int_0^\infty M(s)\mathbf{f}[\mathbf{B}_{t-s}(t)]\mathrm{d}s. \tag{10}$$

By making this change of variable the Finger tensor $\mathbf{B}_{t'}(t)$ does not become exclusively a function of the elapsed time $s = t - t'$, but remains dependent on the present time t although not explicitly. For instance, for a single mode UCM fluid, $m_1 = 1$ in (8), the evolution of the shear stress component $\tau^{xy}(t)$ is given by

$$\tau^{xy}(t) = \int_{-\infty}^{t} \frac{a_1}{\lambda_1} \mathrm{e}^{-\frac{t-t'}{\lambda_1}} B^{xy}_{t'}(t)\mathrm{d}t'. \tag{11}$$

Assuming a flow with a constant shear rate, $\dot\gamma$, the deformation history is given by (cf. [6,33]):

$$B^{xy} = \dot\gamma(t - t'), \quad t > 0, \ \ t' > 0,$$
$$B^{xy} = \dot\gamma t, \quad t > 0, \ \ t' < 0.$$

The integral in Eq. (8) for τ^{xy} can be split into two integrals using the intervals $[-\infty, 0]$ and $[0, t]$, since the Finger tensor takes distinct values. Thus, the stress is given by

$$\tau^{xy}(t) = \int_{-\infty}^{0} \frac{a_1}{\lambda_1} \exp\left(-\frac{t-t'}{\lambda_1}\right)(\dot\gamma t)\mathrm{d}t' + \int_0^t \frac{a_1}{\lambda_1} \exp\left(-\frac{t-t'}{\lambda_1}\right)\dot\gamma(t-t')\mathrm{d}t'. \tag{12}$$

Using this idea, the approach developed in this work takes the time t' as the reference time so that integrals of type (12) are solved at each time-step. The main ideas are taken from Peters et al. [34] and Hulsen et al. [15], namely, the Finger tensor at time t' is computed using

$$\frac{\partial}{\partial t}\mathbf{B}_{t'}(\mathbf{x}, t) + \mathbf{v}(\mathbf{x}, t)\cdot\nabla\mathbf{B}_{t'}(\mathbf{x}, t) = [\nabla\mathbf{v}(\mathbf{x}, t)]^{\mathrm{T}}\cdot\mathbf{B}_{t'}(\mathbf{x}, t) + \mathbf{B}_{t'}(\mathbf{x}, t)\cdot\nabla\mathbf{v}(\mathbf{x}, t). \tag{13}$$

The new methodology proposed here for calculating the extra-stress tensor $\boldsymbol{\tau}(t)$ at time $t = t_n + \delta t$ relies on the following sequence of steps:

(a) Discretization of the time interval $[0, t]$ into a number of time subintervals thus defining a set of integration nodes t'_k, which are intermediate times between 0 and t.
(b) Computation of the Finger tensor at the nodes t'_k, namely, $\mathbf{B}_{t'_k}(t)$.
(c) Calculation of the integral equation (8).

These three steps are based on the ideas of the *deformation fields* introduced by Peters et al. [34], but employing a different approach to be discussed next.

3.1. Discretization of the time interval $[0, t]$

For ease of understanding let us assume the memory function contains a single mode, i.e. a single exponential term, $M(t - t') = \frac{a_1}{\lambda_1 We}\mathrm{e}^{-\frac{(t-t')}{\lambda_1 We}}$. This is a fast decaying function of t and therefore, one should not take equally spaced subintervals in $[0, t]$, but smaller subintervals near the present time t, where the variation of $M(t - t')$ is faster than near $t = 0$, where the variation of $M(t - t')$ is slower. There are many ways of discretizing the interval $[0, t]$ obeying this criterion and here a simple and direct procedure based on the behaviour of the memory function is employed. First, the interval $[M(t), M(0)]$ is split into N equally spaced subintervals obtaining $(N + 1)$ values $M_k = M(t) + k\,\mathrm{d}M$ with $k = 0, 1, 2, \ldots, N$ and $\mathrm{d}M = [M(t) - M(0)]/N$. Next, the inverse image of these memory values is determined leading to $(N + 1)$ values of t'_k given by

$$t'_k(t) = \lambda_1 We \ln\left(\frac{\lambda_1 We}{a_1} M_k\right) + t, \quad k = 0, 1, \ldots, N. \tag{14}$$

For the general case of a multimode memory function the same procedure is applied for each exponential term $M_m = (a_m/(\lambda_m We))\mathrm{e}^{-(t-t')/\lambda_m We}$ leading to a different set of t'_k values for each mode m, expressed by an equation similar to Eq. (14). Since a single set of subintervals is required for all modes, the final values of t'_k are obtained by the simple arithmetic averaging of Eq. (14)

$$t'_k(t) = \frac{\sum_{m=1}^{m_1} t'_{k_m}(t)}{m_1}, \tag{15}$$

where t'_{k_m} is the value obtained for each mode m. Fig. 1 displays how the interval $[0, t]$ is discretized.

This procedure for calculating the integration nodes t'_k is performed at each time-step.

3.2. Computation of the Finger tensor

Henceforth, we will use as much as possible the index notation for compactness. Here repeated indices indicate a sum over all components. Considering that $\nabla \mathbf{v}_{ij} = \frac{\partial u_j}{\partial x_i}$, the ij component of the Finger tensor at time $t = t_n + \delta t$, denoted by $\mathbf{B}^{ij}_{t'_k(t_n)}(t)$, is calculated from the values of $\mathbf{B}^{ij}_{t'_k(t_n)}(t_n)$ using the following equation:

$$\frac{\partial}{\partial t}\mathbf{B}^{ij}_{t'_k(t_n)}(t) + \frac{\partial}{\partial x_l}[u_l \mathbf{B}^{ij}_{t'_k(t_n)}(t)] = \frac{\partial u_i}{\partial x_l}\mathbf{B}^{lj}_{t'_k(t_n)}(t) + \mathbf{B}^{il}_{t'_k(t_n)}(t)\frac{\partial u_j}{\partial x_l} \tag{16}$$

with the condition $\mathbf{B}^{ij}_t(t) = \delta^{ij}$, where δ^{ij} is the Kronecker delta.

Eq. (16) is solved by the explicit Euler method. Thus, given the fields at time t_n, the fields $\mathbf{B}^{ij}_{t'_k(t_n)}(\mathbf{x}, t)$, where $t = t_n + \delta t$, are computed by

$$\mathbf{B}^{ij}_{t'_k(t_n)}(\mathbf{x}, t) = \mathbf{B}^{ij}_{t'_k(t_n)}(\mathbf{x}, t_n) + \delta t\left\{-\frac{\partial[\mathbf{u}_l(\mathbf{x}, t_n)\mathbf{B}^{ij}_{t'_k(t_n)}(\mathbf{x}, t_n)]}{\partial x_l} + \frac{\partial u_i(\mathbf{x}, t_n)}{\partial x_l}\mathbf{B}^{lj}_{t'_k(t_n)}(\mathbf{x}, t_n) + \mathbf{B}^{il}_{t'_k(t_n)}(\mathbf{x}, t_n)\frac{\partial u_j(\mathbf{x}, t_n)}{\partial x_l}\right\}. \tag{17}$$

At this stage the fields at time $t'_k(t_n)$, namely $\mathbf{B}^{ij}_{t'_k(t_n)}(\mathbf{x}, t)$, are known. To calculate $\mathbf{B}^{ij}_{t'_k(t)}(\mathbf{x}, t)$ a second-order polynomial interpolation is used. For example, if $t'_\xi(t) \in [t'_{k-1}(t_n), t'_{k+1}(t_n)]$ then $\mathbf{B}^{ij}_{t'_\xi(t)}(\mathbf{x}, t)$ is calculated by a second-order interpolation using the values of $\mathbf{B}^{ij}_{t'_{k-1}(t_n)}(\mathbf{x}, t)$, $\mathbf{B}^{ij}_{t'_k(t_n)}(\mathbf{x}, t)$ and $\mathbf{B}^{ij}_{t'_{k+1}(t_n)}(\mathbf{x}, t)$ as illustrated in Fig. 2 for the case of simple shear flow, where $B^{xy}_{t'_k(t)} = \dot{\gamma}(t - t')$. For instance, if we use Lagrange interpolation, $\mathbf{B}^{ij}_{t'_\xi(t)}(\mathbf{x}, t)$ is computed by the formula

$$\mathbf{B}^{ij}_{t'_\xi(t)}(\mathbf{x}, t) = l_0(t'_k(t))\mathbf{B}^{ij}_{t'_{k-1}(t_n)} + l_1(t'_k(t))\mathbf{B}^{ij}_{t'_k(t_n)} + l_2(t'_k(t))\mathbf{B}^{ij}_{t'_{k+1}(t_n)}, \tag{18}$$

where $l_0(t'_k(t)), l_1(t'_k(t)), l_2(t'_k(t))$ are the Lagrange polynomials at points $t'_{k-1}(t_n), t'_k(t_n), t'_{k+1}(t_n)$, respectively.

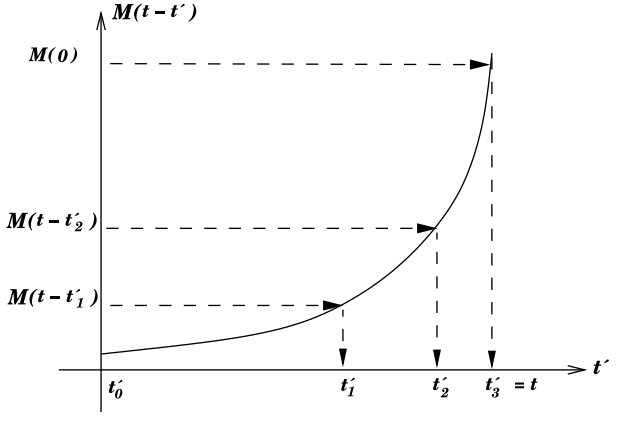

Fig. 1. Discretization of the time interval $[0, t]$. The values t'_k are calculated as the inverse image of $M_k(t)$.

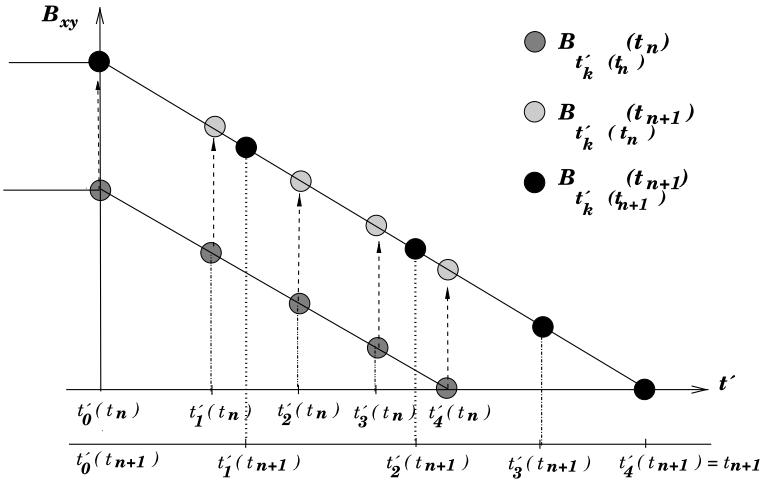

Fig. 2. Calculation of the Finger tensor at times $t'_k(t)$.

This interpolation procedure is important in order to compute the correct value of the Finger tensor. Otherwise, the values of the Finger tensor at $t'_k(t)$ would be approximated by the values at $t'_k(t_n)$, which would cause a large error as time increases (see Fig. 3).

The components of the Finger tensor are calculated and stored at each past time $t'_k, k = 0, 1, \ldots, N$. Eq. (17) is solved by the finite difference method and the corresponding algebraic equations are given in Section 5.

3.2.1. Calculation of the Finger tensor on mesh boundaries

To approximate the derivatives of the Finger tensor in the convective terms of Eq. (17) the high resolution CUBISTA scheme [2] is used. This scheme requires the values of the variables at upstream far neighbour points relative to the point where the derivative is being calculated. For points well within the computational domain the expressions are given by Alves et al. [2] and here only the points near boundaries are discussed.

The flow problems dealt with in this work have orthogonal boundaries aligned with a Cartesian coordinate system and this is considered in the following:

- Rigid boundary
  Using indices t and n to denote tangential and normal directions to the (stationary) wall, respectively, the no-slip condition and the continuity equation imply $u_i = 0; \frac{\partial u_i}{\partial x_t} = 0, \frac{\partial u_n}{\partial x_n} = 0$, so that only the velocity derivative of the tangential velocity in respect to the direction normal to the wall is non-zero ($\frac{\partial u_t}{\partial x_n} \neq 0$). For other quantities in Eq. (16) $\frac{\partial}{\partial x_t} = 0$, leading to

$$\frac{\partial}{\partial t} B^{ij}_{t'_{k(t_n)}}(t) = \frac{\partial u_i}{\partial \mathrm{n}} B^{\mathrm{n}j}_{t'_{k(t_n)}}(t) + B^{\mathrm{in}}_{t'_{k(t_n)}}(t) \frac{\partial u_j}{\partial \mathrm{n}}. \tag{19}$$

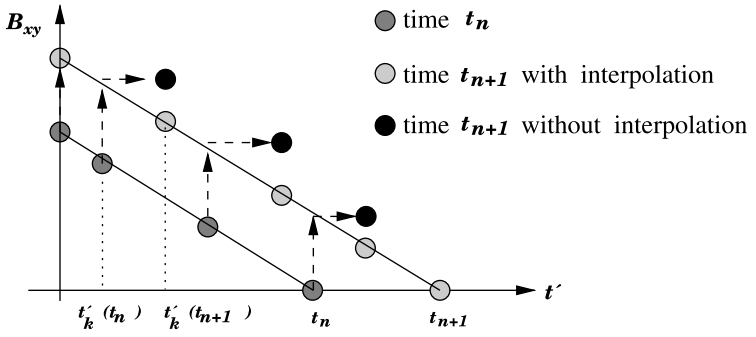

Fig. 3. Calculation of the Finger tensor without interpolation.

- Inflows
  At inflows a fully-developed shear flow is set. If the unitary vector of direction t is embedded in the inflow plane, the differential equation simplifies to

$$\frac{\partial B^{ij}_{t'_{k(t_n)}}(t)}{\partial t} = \frac{\partial u_i}{\partial x_{\mathrm{t}}} B^{\mathrm{t}j}_{t'_{k(t_n)}}(t) + B^{i\mathrm{t}}_{t'_{k(t_n)}}(t)\frac{\partial u_j}{\partial x_{\mathrm{t}}} \quad \text{with } u_t = 0 \text{ and } \frac{\partial}{\partial x_{\mathrm{n}}} = 0,$$

  where n is the direction normal to the inflow plane. For instance, for a two-dimensional flow (e.g. see [6])

$$B^{\mathrm{nn}}_{t'}(t) = \left(\frac{\partial u_{\mathrm{n}}}{\partial t}\right)^2 (t-t')^2 + 1; \quad B^{\mathrm{nt}}_{t'}(t) = \left(\frac{\partial u_{\mathrm{n}}}{\partial t}\right)(t-t'); \quad B^{\mathrm{tt}}_{t'}(t) = 1. \tag{20}$$

  For a 3D flow the other normal component of tensor $\mathbf{B}$ is also unitary, and for the shear components two situations arise: for the component $B^{\mathrm{nt}'}$ where t′ is the special tangential direction along which there is a non-zero velocity gradient, Eq. (20) holds, whereas for the other shear components $B^{it'} = 0$.
- Outflows
  On outflows the homogeneous Neumann condition for the Finger tensor holds. If n denotes a direction normal to the outflow plane, the following condition is set:

$$\frac{\partial B^{ij}_{t'}(t)}{\partial x_{\mathrm{n}}} = 0. \tag{21}$$

3.3. Computation of the extra-stress tensor $\boldsymbol{\tau}(\mathbf{x}, t)$

Having obtained the integration points $t'_k(t)$ and $\mathbf{B}_{t'_k(t)}(\mathbf{x}, t)$, the computation of the stress tensor is performed as follows.

First, the constitutive equation is written as

$$\boldsymbol{\tau}(\mathbf{x}, t) = \int_{-\infty}^{0} M(t-t')\mathbf{f}[\mathbf{B}_{t'}(\mathbf{x}, t)]\mathrm{d}t' + \sum_{k=0}^{\frac{N-2}{2}} \left\{ \int_{t'_{2k}}^{t'_{2k+2}} M(t-t')\mathbf{f}[\mathbf{B}_{t'}(t)]\mathrm{d}t' \right\}, \tag{22}$$

where for the K–BKZ model, the function $\mathbf{f}[\mathbf{B}_{t'}(t)]$ is given by

$$\mathbf{f}[\mathbf{B}_{t'}(\mathbf{x}, t)] = \frac{\alpha \mathbf{B}_{t'}(\mathbf{x}, t)}{\alpha - 3 + \beta I_1 + (1-\beta) I_2}$$

and $\mathbf{f}[\mathbf{B}_{t'}(t)] = \mathbf{B}_{t'}(t)$ if the UCM model is employed. For simplicity, we consider a single mode model $m_1 = 1$ in the memory function (4); the case $m_1 > 1$ is analogous.

For $t' < 0$, $\mathbf{B}_{t'}(\mathbf{x}, t) = \mathbf{B}_0(\mathbf{x}, t)$ is assumed. Thus, the first integral in (22) takes the form of

$$\int_{-\infty}^{0} \frac{a_1}{\lambda_1 We} \mathrm{e}^{-\frac{t-t'}{\lambda_1 We}} \mathbf{f}[\mathbf{B}_{t'_0}(\mathbf{x}, t)]\mathrm{d}t' \tag{23}$$

and can be solved exactly because $\mathbf{f}[\mathbf{B}_{t'_0}(\mathbf{x}, t)]$ is a constant.

The integrals in the summation are solved by a second-order integration formula using the method of undetermined coefficients, leading to the following expression:

$$\int_{t'_{2k}}^{t'_{2k+2}} M(t-t')\mathbf{f}[\mathbf{B}_{t'}(t)]\mathrm{d}t' = \sum_{j=1}^{3} A_j \mathbf{f}[\mathbf{B}_{t'_{2k+j-1}}(t)], \tag{24}$$

where the coefficients A_j $(j = 1, 2, 3)$ are the solution of the following linear system of equations (see [16]):

$$\begin{cases} I_3(1) = A_1 + A_2 + A_3 = b_1, \\ I_3(t') = A_1 t'_{2k} + A_2 t'_{2k+1} + A_3 t'_{2k+2} = b_2, \\ I_3(t'^2) = A_1 t'^2_{2k} + A_2 t'^2_{2k+1} + A_3 t'^2_{2k+2} = b_3, \end{cases} \tag{25}$$

where

$$b_1 = \int_{t'_{2k}}^{t'_{2k+2}} \frac{1}{\lambda_1} e^{\frac{-(t-t')}{\lambda_1}} dt' = a_1 \left[e^{\frac{(t'_{2k+2}-t)}{\lambda_1}} - e^{\frac{(t'_{2k}-t)}{\lambda_1}} \right],$$

$$b_2 = \int_{t'_{2k}}^{t'_{2k+2}} \frac{1}{\lambda_1} e^{\frac{-(t-t')}{\lambda_1}} t' dt' = a_1 \left[(t'_{2k+2} - \lambda_1) e^{\frac{(t'_{2k+2}-t)}{\lambda_1}} - (t'_{2k} - \lambda_1) e^{\frac{(t'_{2k}-t)}{\lambda_1}} \right],$$

$$b_3 = \int_{t'_{2k}}^{t'_{2k+2}} \frac{1}{\lambda_1} e^{\frac{-(t-t')}{\lambda_1}} t'^2 dt' = a_1 \left\{ t'^2_{2k+2} e^{\frac{(t'_{2k+2}-t)}{\lambda_1}} - t'^2_{2k} e^{\frac{(t'_{2k}-t)}{\lambda_1}} - 2\lambda_1 \left[(t'_{2k+2} - \lambda_1) e^{\frac{(t'_{2k+2}-t)}{\lambda_1}} - (t'_{2k} - \lambda_1) e^{\frac{(t'_{2k}-t)}{\lambda_1}} \right] \right\}.$$

The solution of this linear system is given by

$$A_3 = \frac{(b_3 - t'^2_{2k} b_1) - (b_2 - t'_{2k} b_1)(t'_{2k+1} + t'_{2k})}{(t'_{2k} - t'_{2k+2})(t'_{2k+1} - t'_{2k+2})},$$

$$A_2 = \frac{(b_2 - t'_{2k} b_1) - (t'_{2k+2} - t'_{2k}) A_3}{t'_{2k+1} - t'_{2k}},$$

$$A_1 = b_1 - (A_2 + A_3).$$

4. Numerical method

Even though the implementation and the calculations in this paper are for two-dimensional Cartesian flows, this description of the numerical method is general. Eqs. (6)–(9) are solved following the ideas of Tomé et al. [45], which are briefly described next. The momentum and mass conservation equations are solved using a projection method followed by the solution of the constitutive equation for the extra-stress tensor according to the following algorithm.

Given the velocity field $u_i(\mathbf{x}, t_n)$, the extra-stress tensor at time t_n, and the corresponding boundary conditions, the following sequence of steps computes the velocity, pressure and extra-stress tensor fields at time $t_{n+1} = t_n + \Delta t$:

Step 1: Calculate an intermediate velocity field, $\tilde{u}_i(\mathbf{x}, t_{n+1})$, from

$$\frac{\partial \tilde{u}_i}{\partial t} = -\frac{\partial}{\partial x_l}(u_l u_i) + \frac{1}{Re}\frac{\partial}{\partial x_l}\left(\frac{\partial u_i}{\partial x_l}\right) + \frac{\partial S^{il}}{\partial x_l} \tag{26}$$

with $\tilde{u}_i(\mathbf{x}, t_n) = u_i(\mathbf{x}, t_n)$ using the correct boundary conditions for $\tilde{u}_i(\mathbf{x}, t_{n+1})$. It can be shown that $\tilde{u}_i(\mathbf{x}, t_{n+1})$ possesses the correct vorticity at time t_{n+1} (see [46]). However, $\frac{\partial \tilde{u}_l}{\partial x_l} \neq 0$ so that there exists a potential function $\psi(\mathbf{x}, t_{n+1})$ such that $u_l(\mathbf{x}, t_{n+1}) = \tilde{u}_l(\mathbf{x}, t_{n+1}) - \frac{\partial \psi(\mathbf{x}, t_{n+1})}{\partial x_l}$ where by continuity

$$\frac{\partial}{\partial x_l}\left(\frac{\partial \psi(\mathbf{x}, t_{n+1})}{\partial x_l}\right) = \frac{\partial \tilde{u}_l(\mathbf{x}, t_{n+1})}{\partial x_l}. \tag{27}$$

Step 2: Solve the Poisson equation (27) with the condition $\frac{\partial \psi}{\partial n} = 0$ on rigid boundaries and inflows and $\psi = 0$ on outflows.

Step 3: Compute the new velocity vector field

$$u_i(\mathbf{x}, t_{n+1}) = \tilde{u}_i - \frac{\partial \psi(\mathbf{x}, t_{n+1})}{\partial x_i}. \tag{28}$$

Step 4: Compute the pressure field

$$p(\mathbf{x}, t_{n+1}) = \frac{\psi(\mathbf{x}, t_{n+1})}{\Delta t}. \tag{29}$$

Step 5: Compute the stress-tensor field $\boldsymbol{\tau}(\mathbf{x}, t_{n+1})$ by the following steps:

5.1 Calculate the integration nodes $t'_k(t), k = 1, \ldots, N$, using the procedure described in Section 3.1

5.2 Compute the components of the Finger tensor on rigid boundaries, inflows and outflows according to the equations presented in Section 3.2.1.
5.3 Calculate the components of the new Finger tensor $\mathbf{B}_{i'}^{ij}(\mathbf{x}, t_{n+1})$ from Eq. (17) (see Section 3.2).
5.4 Compute the components of the new extra-stress tensor $\boldsymbol{\tau}(\mathbf{x}, t_{n+1})$ from (22) (see Section 3.3).

Step 6: Compute the components of the new tensor $\mathbf{S}(\mathbf{x}, t_{n+1})$ by using (9).

5. Basic finite difference equations

For solving numerically the equations presented in Section 4 a finite difference method is used with a staggered grid, having cell spacings Δx and Δy, to ensure coupling between the velocity and pressure fields. Fig. 4(a) displays the position of the variables in a given cell. The momentum equations for the velocity components u and v are solved at the cell faces $(i+\frac{1}{2}, j)$ and $(i, j+\frac{1}{2})$, respectively, whereas the equations for the pressure, the extra-stress tensor, the Finger tensor and the non-Newtonian tensor $\mathbf{S}$ are calculated at cell centres. The flow domain is mapped by an orthogonal Cartesian mesh having four types of cells, as schematically shown in Fig. 4(b) for a two-dimensional flow, which can be described as

- Full (**F**) cell – Interior cells full of fluid.
- Boundary (**B**) cell – Cells that define a rigid boundary. In these cells the no-slip condition is applied and the Finger tensor is calculated according to the equations derived in Section 3.2.1.
- Inflow (**I**) cell – Cells that define an inflow boundary.
- Outflow (**O**) cell – Cells that define an outflow boundary.

The equations referred to in Steps 1–4 of the previous section are identical to those used for computing the flow of an Oldroyd-B fluid and the corresponding finite difference equations have already been presented by Tomé et al. [45]. Therefore, here only the finite difference equations for calculating Steps 5 and 6 are described in the following sub-sections.

5.1. Approximation of the Finger tensor

To calculate the Finger tensor from Eq. (16) the time derivative is discretized using the explicit Euler method, the velocity gradients are computed by central differences and for the convective terms the CUBISTA high resolution scheme [2] is used. Details of the implementation of the CUBISTA scheme for two-dimensional flows can be found in [8]. Therefore, the component B^{pq} of the Finger tensor is calculated by

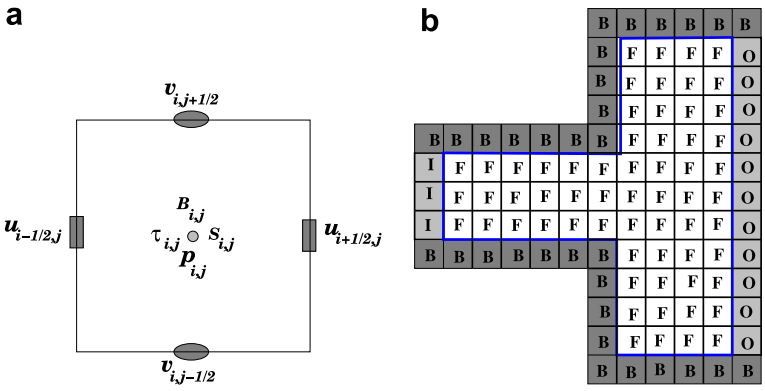

Fig. 4. (a) Typical cell for fluid flow calculation, and (b) types of cells within the mesh. The cells describing the type of boundary (**I**, **B**, **O**) lie outside the flow domain.

$$B^{pq}_{t'_k(t_n)}(t_{n+1}) = B^{pq}_{t'_k(t_n)}(t_n) + \Delta t\left\{-\frac{\partial}{\partial x_l}\left[u_l B^{pq}_{t'_k(t_n)}(t_n)\right] + \left.\frac{\partial u_p}{\partial x_l}\right|_{i,j} B^{lq}_{t'_k(t_n)}(t_n)|_{i,j} + B^{pl}_{t'_k(t_n)}(t_n)|_{i,j}\left.\frac{\partial u_q}{\partial x_l}\right|_{i,j}\right\} \tag{30}$$

(in Eq. (30), no summation over column of index i and row of index j in the mesh) where

$$\left.\frac{\partial u_p}{\partial x_l}\right|_{i,j} = \frac{u_p^{f^+} - u_p^{f^-}}{\Delta x_l},$$

where $u_p^{f^+}$ indicates the value of the velocity component u_p at the positive face of the cell (i,j) in the direction l. According to Fig. 4(a), f^+ in the direction x is represented by the subscript $(i+\frac{1}{2},j)$.

Velocities which are not defined at the centre of a cell face are obtained by arithmetic averaging the nearest neighbours in all directions. For instance

$$u_{i,j+\frac{1}{2}} = 0.25\left(u_{i+\frac{1}{2},j} + u_{i+\frac{1}{2},j+1} + u_{i-\frac{1}{2},j} + u_{i-\frac{1}{2},j+1}\right).$$

Eq. (30) is solved for each full cell (i,j) for each past time $t'_k(t_n), k = 0,1,\ldots,N$ and it convects the deformation fields $\mathbf{B}_{t'_k(t_n)}(t_n)$ at past times $t'_k(t_n)$ to the next time level $t = t_{n+1}$. Having calculated $\mathbf{B}_{t'_k(t_n)}(t_{n+1})$, the new values of $t'_k(t_{n+1})$ in the interval $[0,t_{n+1}]$ are obtained using the procedure described in Section 3.1 and the values of $\mathbf{B}_{t'_k(t_{n+1})}(t_{n+1})$ are then computed by a second-order interpolation using Eq. (18).

5.1.1. Approximation of the Finger tensor on mesh boundaries

To compute the advective terms of Eq. (30), the values of the Finger tensor on the centre of the boundary cells (cells **B**, **I** and **O** in Fig. 4(b)) are required and they are obtained as follows:

- *Rigid boundaries*: These boundaries are identified by boundary cells (**B**) which have one face in contact with an interior cell (**F**). For instance, if a **B** cell has the right (or left) face in contact with an **F**-cell (see Fig. 5(a)) then we assume that the rigid boundary is vertical passing on the $(i+\frac{1}{2})$-face (or $(i-\frac{1}{2})$-face) of the **B**-cell and compute the components of the Finger tensor on the centre of this face from Eq. (19) which are approximated by

$$B^{\mathrm{nn}}_{t'}(t_{n+1})|_{(i+\frac{1}{2},j)} = 1, \tag{31}$$

$$B^{\mathrm{nt}}_{t'}(t_{n+1})|_{(i+\frac{1}{2},j)} = B^{\mathrm{nt}}_{t'}(t_n)|_{(i+\frac{1}{2},j)} + \delta t\frac{\partial u^{\mathrm{t}}}{\partial x_{\mathrm{n}}}(t_{n+1})|_{(i+\frac{1}{2},j)}, \tag{32}$$

$$B^{\mathrm{tt}}_{t'}(t_{n+1})|_{(i+\frac{1}{2},j)} = B^{\mathrm{tt}}_{t'}(t_n)|_{(i+\frac{1}{2},j)} + 2\delta t\frac{\partial u^{\mathrm{t}}}{\partial x_{\mathrm{n}}}(t_{n+1})|_{(i+\frac{1}{2},j)} B^{\mathrm{nt}}_{t'}(t_n)|_{(i+\frac{1}{2},j)}, \tag{33}$$

where the superscripts t and n denote directions tangent and normal to the rigid boundary, respectively. The velocity derivative $\frac{\partial u^{\mathrm{t}}}{\partial x_{\mathrm{n}}}$ is calculated by the second-order formulae

$$\frac{\partial u^{\mathrm{t}}}{\partial x_{\mathrm{n}}}(t_{n+1})|_{(i+\frac{1}{2},j)} = (3u^{\mathrm{t}}_{i+1,j} - u^{\mathrm{t}}_{i+2,j}/3)/\delta x_{\mathrm{n}},$$

where the velocities $u^{\mathrm{t}}_{i+1,j}$ and $u^{\mathrm{t}}_{i+2,j}$ are obtained by averaging the two nearest grid values, namely,

$$u^{\mathrm{t}}_{i+1,j} = \frac{v_{i+1,j+\frac{1}{2}} + v_{i+1,j-\frac{1}{2}}}{2}, \quad u^{\mathrm{t}}_{i+2,j} = \frac{v_{i+2,j+\frac{1}{2}} + v_{i+2,j-\frac{1}{2}}}{2}.$$

The components of the Finger tensor at the centre of cell are then obtained by linear extrapolation between the points $(i+1/2,j)$ and $(i+1,j)$, which gives

$$B^{pq}_{t'}(t_{n+1})|_{(i,j)} = 2B^{pq}_{t'}(t_{n+1})|_{(i+\frac{1}{2},j)} - B^{pq}_{t'}(t_n)|_{(i+1,j)}. \tag{34}$$

The case of a **B**-cell having the $(j+\frac{1}{2})$-face or the $(j-\frac{1}{2})$-face in contact with a **F**-cell face is treated similarly.

- *Corners*: It may happen that the contour changes its direction abruptly; in this case, a **B**-cell would have two adjacent faces in contact with **F**-cells faces (see Fig. 5(b)). For these cells the components of the

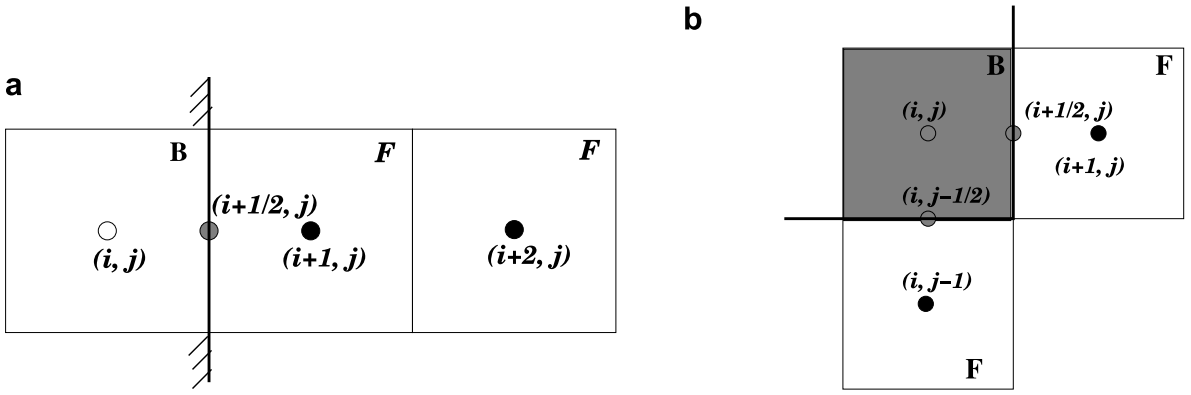

Fig. 5. Computation of the components of the Finger tensor at the centre of the boundary cell $\mathbf{B}_{i,j}$.

Finger tensor are first calculated on both faces of the **B**-cell in contact with the **F**-cell faces and interpolated to the centre of the **B**-cell in the two directions. The components of the Finger tensor at the centre of the **B**-cell are then computed by averaging the values obtained at the centre of the **B**-cell in the two directions.

5.2. Time-step calculation

A time-stepping procedure for computing the time-step size for every calculational cycle is employed. It is based on the following stability conditions (written in non-dimensional form):

$$\delta t_1 < \frac{\delta \mathbf{x}}{\mathbf{u}}, \tag{35}$$

$$\delta t_2 < \alpha\, \delta t_{\text{Newt}} \frac{1}{We} \quad \text{if } We \geqslant 1, \tag{36}$$

$$\delta t_2 < \alpha\, \delta t_{\text{Newt}} \quad \text{if } We < 1, \tag{37}$$

where $0 < \alpha < 1$ and

$$\delta t_{\text{Newt}} = \begin{cases} \frac{1}{2} \frac{\delta r^2\, \delta z^2}{\delta r^2 + \delta z^2} Re & \text{if } Re < 1, \\ \frac{1}{2} \frac{\delta r^2\, \delta z^2}{\delta r^2 + \delta z^2} & \text{otherwise.} \end{cases}$$

Eq. (35) is understood componentwise. The time-step employed in the calculation is $\delta t = \text{FACT} \min\{\delta t_1, \delta t_2\}$ where $\text{FACT} < 1$. The implementation of these equations follows the same ideas used by GENSMAC (see [47]).

6. Validation of the extra-stress calculation

To validate the numerical procedure for the extra-stress tensor calculation, predictions are carried out for steady shear and elongational uniaxial flows for which there are analytic solutions for the UCM model. For steady shear flow, the components of the extra-stress tensor τ^{xy} and τ^{yy} will not be computed because the components of the Finger tensor are first degree polynomials for which the Euler method provides the exact solution. Regarding uniaxial elongational flow, the error in the component τ^{yy} was much smaller than the error for the component τ^{xx} and for this reason only these will be presented.

The errors obtained by the numerical method are a function of the shear rate $\dot{\gamma}$ and of the elongation rate $\dot{\varepsilon}$, for a given λ. The number of fields, $\mathbf{B}_{t'_k}(t)$, will be varied by changing the number of subintervals, N, in $[0, t]$.

For both steady flows the Finger tensor is calculated by introducing the velocity field into Eq. (16). For shear flows, the following expressions are obtained:

$$\begin{array}{ccc} \text{(i)} & \text{(ii)} & \text{(iii)} \\ \begin{cases} u = \dot{\gamma} y, \\ v = 0, \\ w = 0, \end{cases} & \begin{cases} \frac{\partial}{\partial t} B^{yy}_{t'} = 0, \\ \frac{\partial}{\partial t} B^{xy}_{t'} = \dot{\gamma} B^{yy}_{t'}, \\ \frac{\partial}{\partial t} B^{xx}_{t'} = 2\dot{\gamma} B^{xy}_{t'}, \end{cases} & \mathbf{B}_{t'}(t) = \begin{pmatrix} 1 + \dot{\gamma}^2 (t-t')^2 & \dot{\gamma}(t-t') & 0 \\ \dot{\gamma}(t-t') & 1 & 0 \\ 0 & 0 & 1 \end{pmatrix}. \end{array} \tag{38}$$

For negative values of t' the Finger tensor is assumed to be $\mathbf{B}_0(t)$. In this case, the exact solution for the extra-stress tensor can now be obtained by solving the integrals:

$$\tau^{xx}(t) = \int_{-\infty}^{0} \frac{a_1}{\lambda_1} \exp\left(-\frac{t-t'}{\lambda_1}\right)(1 + \dot{\gamma}^2 t^2)\mathrm{d}t' + \int_0^t \frac{a_1}{\lambda_1} \exp\left(-\frac{t-t'}{\lambda_1}\right)(1 + \dot{\gamma}^2 (t-t')^2)\mathrm{d}t', \tag{39}$$

$$\tau^{xy}(t) = \int_{-\infty}^{0} \frac{a_1}{\lambda_1} \exp\left(-\frac{t-t'}{\lambda_1}\right)(\dot{\gamma} t)\mathrm{d}t' + \int_0^t \frac{a_1}{\lambda_1} \exp\left(-\frac{t-t'}{\lambda_1}\right)\dot{\gamma}(t-t')\mathrm{d}t', \tag{40}$$

$$\tau^{yy}(t) = \tau^{zz}(t) = \int_{-\infty}^{0} \frac{a_1}{\lambda_1} \exp\left(-\frac{t-t'}{\lambda_1}\right)\mathrm{d}t' + \int_0^t \frac{a_1}{\lambda_1} \exp\left(-\frac{t-t'}{\lambda_1}\right)\mathrm{d}t', \tag{41}$$

leading to the following stress fields:

$$\tau^{xx}(t) = a_1 \mathrm{e}^{\frac{-t}{\lambda_1}}(1 + \dot{\gamma}^2 t^2) + a_1(1 - \mathrm{e}^{\frac{-t}{\lambda_1}}) + a_1 \dot{\gamma}^2 \left[2\lambda_1^2 - \mathrm{e}^{\frac{-t}{\lambda_1}}(t^2 + 2\lambda_1 t + 2\lambda_1^2)\right], \tag{42}$$

$$\tau^{xy}(t) = a_1 \dot{\gamma} \lambda_1 \left(1 - \mathrm{e}^{\frac{-t}{\lambda_1}}\right), \tag{43}$$

$$\tau^{yy}(t) = \tau^{zz}(t) = a_1. \tag{44}$$

For the uniaxial elongational flow we have

$$\begin{array}{ccc} \text{(i)} & \text{(ii)} & \text{(iii)} \\ \begin{cases} u = \dot{\varepsilon} x, \\ v = -\frac{1}{2}\dot{\varepsilon} y, \\ w = -\frac{1}{2}\dot{\varepsilon} z, \end{cases} & \begin{cases} \frac{\partial}{\partial t} B^{xx}_{t'} = 2\dot{\varepsilon} B^{xx}_{t'}, \\ \frac{\partial}{\partial t} B^{yy}_{t'} = -\dot{\varepsilon} B^{yy}_{t'}, \end{cases} & \mathbf{B}_{t'}(t) = \begin{pmatrix} \mathrm{e}^{2\dot{\varepsilon}(t-t')} & 0 & 0 \\ 0 & \mathrm{e}^{-\dot{\varepsilon}(t-t')} & 0 \\ 0 & 0 & \mathrm{e}^{-\dot{\varepsilon}(t-t')} \end{pmatrix}. \end{array} \tag{45}$$

Again, as for shear flows, for negative values of t' the Finger tensor is set to that at $t' = 0$. The extra-stress tensor is calculated by solving the integrals

$$\tau^{xx}(t) = \int_{-\infty}^{0} \frac{a_1}{\lambda_1} \mathrm{e}^{\left(-\frac{t-t'}{\lambda_1}\right)} \mathrm{e}^{2\dot{\varepsilon} t}\,\mathrm{d}t' + \int_0^t \frac{a_1}{\lambda_1} \mathrm{e}^{\left(-\frac{t-t'}{\lambda_1}\right)} \mathrm{e}^{2\dot{\varepsilon}(t-t')}\,\mathrm{d}t', \tag{46}$$

$$\tau^{yy}(t) = \tau^{zz}(t) = \int_{-\infty}^{0} \frac{a_1}{\lambda_1} \mathrm{e}^{\left(-\frac{t-t'}{\lambda_1}\right)} \mathrm{e}^{-\dot{\varepsilon} t}\,\mathrm{d}t' + \int_0^t \frac{a_1}{\lambda_1} \mathrm{e}^{\left(-\frac{t-t'}{\lambda_1}\right)} \mathrm{e}^{-\dot{\varepsilon}(t-t')}\,\mathrm{d}t', \tag{47}$$

which gives

$$\tau^{xx}(t) = a_1 \exp\left(\frac{-t(1 - 2\lambda_1\dot{\varepsilon})}{\lambda_1}\right)\left[1 - \frac{1}{1 - 2\lambda_1\dot{\varepsilon}}\right] + \frac{a_1}{1 - 2\lambda_1\dot{\varepsilon}}, \tag{48}$$

$$\tau^{yy}(t) = a_1 \exp\left(-\frac{t(1 + \lambda_1\dot{\varepsilon})}{\lambda_1}\right)\left[1 - \frac{1}{1 + \lambda_1\dot{\varepsilon}}\right] + \frac{a_1}{1 + \lambda_1\dot{\varepsilon}}. \tag{49}$$

For these flows, the component τ^{xx} grows with time and exhibits a singularity at $\lambda_1\dot{\varepsilon} = \frac{1}{2}$. To keep τ^{xx} bounded, values of λ_1 and $\dot{\varepsilon}$ will be used so that $\lambda_1\dot{\varepsilon} < \frac{1}{2}$.

The methodology described in Sections 3.1–3.3 for obtaining numerically the components of the extra-stress tensor was applied to shear and elongational flows and the numerical predictions were compared with the corresponding analytic solutions in Figs. 6 and 7.

Figs. 6 and 7 show the relative error in the computation of the stress component τ^{xx} for shear and uniaxial elongational flows at time $t = 10\lambda_1$. The model parameters were $a_1 = 100$ Pa and $\lambda_1 = 1$ s, the time-step size

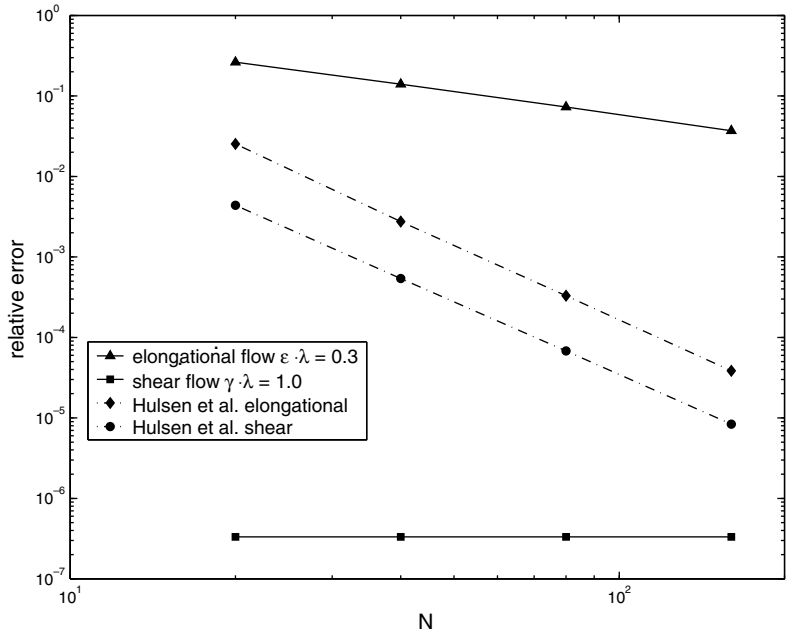

Fig. 6. Relative error in the computation of τ^{xx} at time $t = 10\lambda_1$ as a function of N. The shear rate is $\dot{\gamma} = 1\ \mathrm{s}^{-1}$, the strain rate is $\dot{\varepsilon} = 0.3\ \mathrm{s}^{-1}$ and $\lambda_1 = 1$ s.

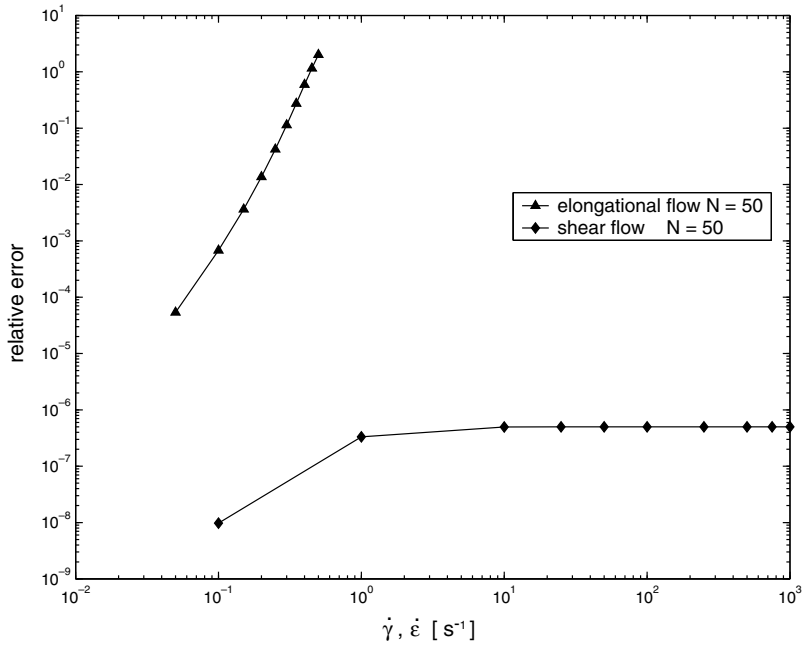

Fig. 7. Relative error in the computation of τ^{xx} for shear and elongational flows as a function of $\dot{\gamma}$ and $\dot{\varepsilon}$. The number of fields $N = 50$ and the relaxation time $\lambda_1 = 1$ s were kept constant.

used in the explicit Euler method was $\delta t = 10^{-6}$ s and the shear rate and the elongation rate were kept fixed at $\dot{\gamma} = 1\ \mathrm{s}^{-1}$ and $\dot{\varepsilon} = 0.3\ \mathrm{s}^{-1}$, respectively. Fig. 6 shows a reduction in error directly proportional to the number of fields N. However, for shear flow the error is constant because, in this case, the component B^{xx} of the Finger

tensor is a second-order polynomial which is exactly captured by the used interpolation scheme and the quadrature formula. Therefore, τ^{xx} in this shear flow is independent of N and the only contribution to the error comes from the numerical solution of the Finger tensor $\mathbf{B}_{t'(t_n)}(t)$ by Eq. (38) using the explicit Euler method. In Fig. 6, our numerical predictions are also compared with the results of Hulsen et al. [15]: for shear flows the errors obtained using our method are much smaller than the errors obtained by their method, whereas for the extensional flow their method is of higher order and consequently, their errors decay faster with N than ours. We believe that the main reason for this behaviour lies in the way the subintervals are considered. In our case, the interval $[0, t_{n+1}]$ is discretized every time-step so that the new integration points $t'_k(t_{n+1}), k = 1, \ldots, N$ are recalculated. Due to the fast decaying memory function $M(t - t')$, if t_{n+1} is large than the first interval $[0, t'_1(t_{n+1})]$ can become very large and the interpolation formulae may not produce accurate approximations in this case. Hulsen et al. dealt with this situation by neglecting this first interval every time a new interval is created (for detail see [34]). We believe Hulsen et al. procedure may not be effective for general flows and for this reason we did not adopt their procedure. However, we have been investigating a more adequate procedure for discretizing the interval $[0, t_{n+1}]$ so that subintervals having large lengths are avoided.

7. Validation and convergence results

The finite difference equations described in Section 5 were implemented into the FreeFlow2D code [30] to simulate two-dimensional flows governed by the integral Upper-Convected Maxwell and K–BKZ constitutive equations. In this section, predictions of channel and contraction flows are presented and compared with literature data, when available.

7.1. Upper-convected Maxwell model

The first validation is carried out for two-dimensional channel flow of an UCM fluid. As shown in Fig. 8, the channel width is L, its length is $10L$, and other input data are

- *Velocity scale*: $U = 1\ \mathrm{ms}^{-1}$, Length scale: $L = 0.01$ m,
- *Kinematic viscosity*: $v_0 = \eta_0/\rho_0 = 0.01\ \mathrm{m}^2\ \mathrm{s}^{-1}$.
- *Maxwell model parameters*: $a_1 = 1000$ Pa and $\lambda_1 = 0.01$ s,
- *Error tolerance for the Poisson equation*: $\mathrm{EPS} = 10^{-10}$,
- *Number of fields*: $N = 50$.

For these parameters we get $Re = UL/v_0 = 1$ and $We = \lambda_1 U/L = 1$. At inflow, the velocity was defined by the parabolic profile

$$u(y) = -4(y - 0.5)^2 + 1 \tag{50}$$

and the Finger tensor was calculated using Eq. (20). It can be shown that in this case, the components of the extra-stress tensor are also given by Eqs. (42)–(44).

We point out that under steady state conditions these analytic solutions are valid at any cross section of the channel.

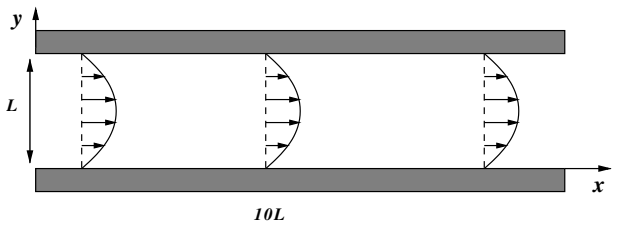

Fig. 8. Flow in a two-dimensional channel: domain description.

To demonstrate the convergence with mesh refinement of the numerical method presented in this paper, the channel flow was simulated using four consecutively refined meshes: mesh **M1** with 10×100 cells, mesh **M2** with 20×200 cells, mesh **M3** with 30×300 cells and mesh **M4** with 40×400 cells.

The simulations started with the channel full of fluid at rest and the Finger tensor was assigned the value 1.

FreeFlow2D simulated this problem until $t = 100$ s after which the contour lines of velocity and stress were seen to be parallel indicating that steady state had been reached (for reasons of space these plots are not shown).

To demonstrate the convergence of the numerical method the predictions obtained on the four meshes were compared with the corresponding analytic solution at the cross section in the middle of the channel ($x = 5L$). These results are displayed in Figs. 9–11 and show differences of less than 1% for mesh **M4**. Moreover, as the mesh is refined the error between the numerical solution and the analytic solution decreases so that we can conclude that the numerical method developed in this work converges towards the true solution.

7.2. K–BKZ model

The numerical technique presented in Section 3 has been applied to simulate the flow in a two-dimensional channel using the integral K–BKZ constitutive equation. The flow input data were the same as for the UCM flow and the K–BKZ parameters used were those employed by Quinzani et al. [38] in the experimental study of the flow in a planar contraction of a Boger fluid (see Table 1). The velocity scale was $U = 0.167$ m s^{-1}, leading to $We = 1$ and $Re = 0.94$. Again, the FreeFlow2D code simulated this problem using meshes **M1**, **M2** and **M3** until steady state was reached.

There is no available analytic solution for this problem so the solutions obtained on meshes **M1** and **M2** are compared with the solution obtained on the finer mesh **M3**. The results obtained for the velocity u and the extra-stress component τ^{xx} are shown in Fig. 12, where we observe good convergence with mesh refinement. Similar results were obtained for the shear stress τ^{xy} and the normal component τ^{yy} (not shown for compactness).

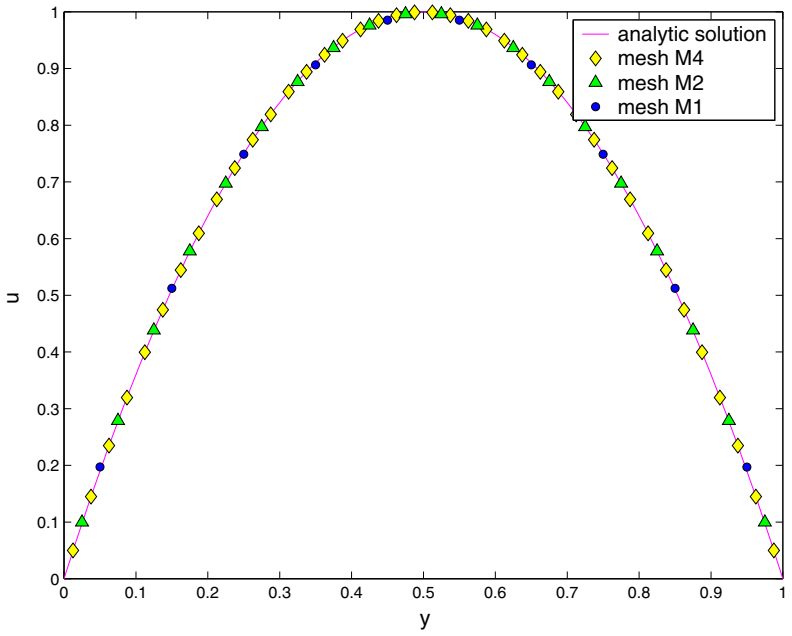

Fig. 9. Numerical and analytic solutions of velocity u at time $t = 100$ s at position $x = 5L$. The solid line represents the analytic solution while the numerical solutions are represented by symbols.

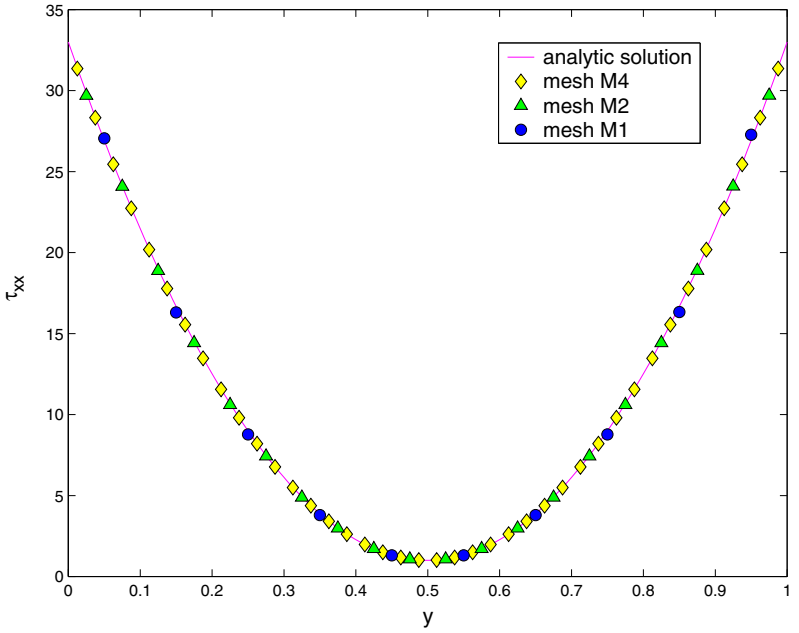

Fig. 10. Numerical and analytic solutions of τ^{xx} at time $t = 100$ s at position $x = 5L$. The solid line represents the analytic solution while the numerical solutions are represented by symbols.

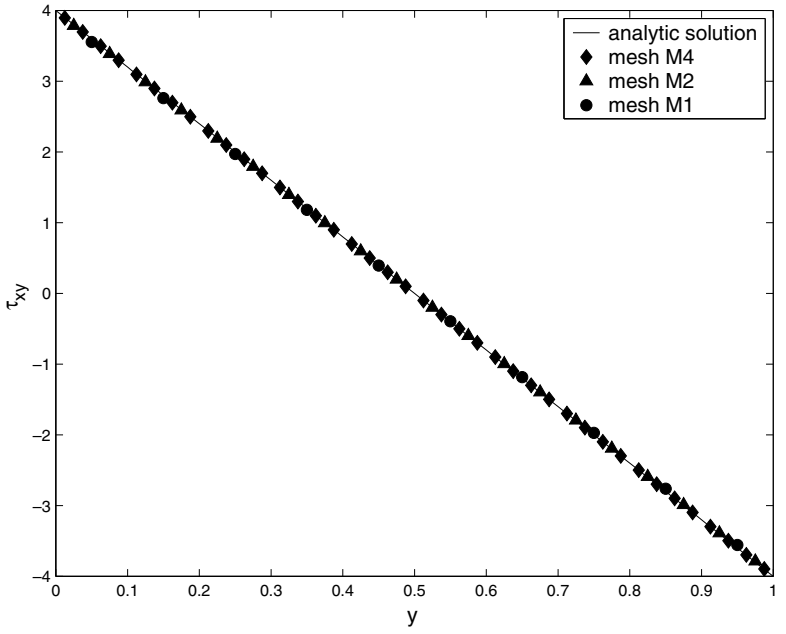

Fig. 11. Numerical and analytic solutions of τ^{xy} at time $t = 100$ s at position $x = 5L$. The solid line represents the analytic solution while the numerical solutions are represented by symbols.

7.3. Comparison with experimental results: K–BKZ fluid

The constitutive model K–BKZ was also used to predict the flow through a 4:1 planar contraction and the numerical results are compared with the experimental data of Quinzani et al. [37]. These authors employed

Table 1
Parameters for the K–BKZ model of the fluid studied by Quinzani et al. [38]: $\alpha = 10$, $\beta = 0.7$ (from [24]), $\eta_0 = 1.424$ Pa s, $\lambda_0 = 0.06$ s

k	λ_k (s)	η_k (Pa s)	a_k (Pa)
1	0.6855	0.040	0.058352
2	0.1396	0.2324	1.664756
3	0.0389	0.5664	14.560411
4	0.0059	0.585	99.152542

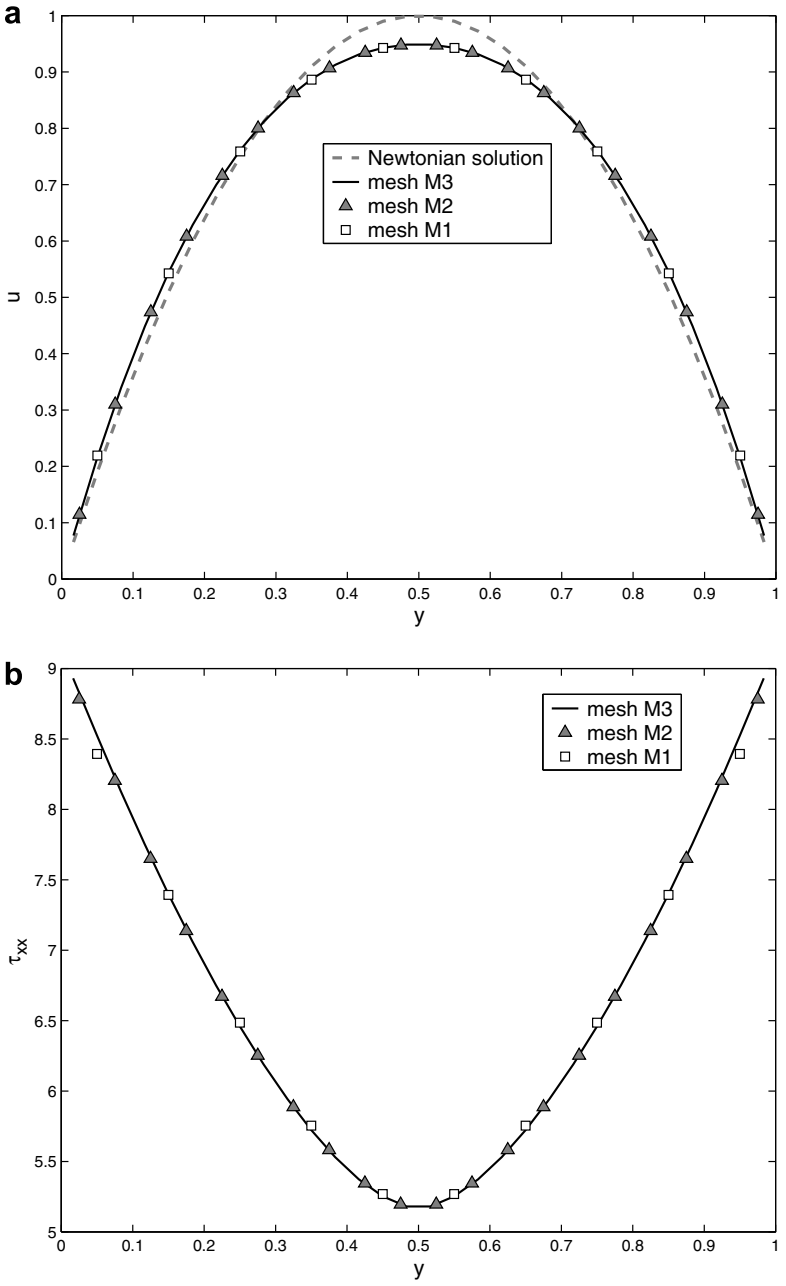

Fig. 12. Numerical simulation of channel flow using the K–BKZ model: $Re = 0.94$ and $We = 1$. Results obtained on meshes **M1**, **M2** and **M3** at the middle of the channel ($x = 5L$). (a) Velocity u, (b) extra-stress component τ^{xx}.

laser-Doppler velocimetry and flow-induced birefringence techniques to measure the velocity and stress fields of the flow in a planar 3.97:1 contraction of a 5 wt% solution of polyisobutylene in tetradecane. The rheology of this fluid was extensively characterized by Quinzani et al. [38], over a range of temperatures, in steady and transient shear flows and the data fitted by several four-mode viscoelastic models, namely the Oldroyd-B, Giesekus and Bird–DeAguiar models. Azaiez et al. [4] used the same experimental data to validate their numerical technique, but using the Giesekus, FENE-P and PTT constitutive equations, and obtained good qualitative agreement between their predictions and the experimental results. Also for the same fluid, Mitsoulis [24] determined the parameters α and β used to fit its rheology with the K–BKZ equation ($\alpha = 10$ and $\beta = 0.7$). The four-mode linear viscoelastic spectrum for this fluid is well predicted using the set of parameters a_k in Table 1 ($a_k = \frac{\eta_k}{\lambda_k}$) which will also be used here during the validation against Quinzani's data.

Using the parameters of Table 1, and the values of α, β given by Mitsoulis [24], the material functions $\eta = \frac{\tau^{xy}}{\dot{\gamma}}$ and $\Psi_1 = \frac{\tau^{xx}-\tau^{yy}}{\dot{\gamma}^2}$ were computed using the numerical method described in Section 3, as a function of the shear rate $\dot{\gamma}$ and compared with Quinzani et al. [38] data in Fig. 13. The predicted steady shear rheology is in good agreement with the experimental data of Quinzani et al. [38]. In addition, the material functions $\eta^+(t,\dot{\gamma}) = \frac{\tau^{xy}(t)}{\dot{\gamma}}$ and $\Psi_1^+(t,\dot{\gamma}) = \frac{\tau^{xx}(t)-\tau^{yy}(t)}{\dot{\gamma}^2}$ were also computed and these predictions are compared in Fig. 14 with Quinzani's data showing again good agreement, especially for large times and large values of the shear rate.

The following predictions concern the flow of a K–BKZ fluid through a planar 4:1 contraction having a downstream half-width of $h = 0.32$ cm (see Fig. 15). This is the experimental setup of Quinzani et al. [37], where the length of the inflow was $2H = 2.54$ cm; here the value used was $2H = 2.56$ cm in order to define a 4:1 contraction ratio.

In order to compare the numerical results with the experimental data of Quinzani et al. [37], the stress and the velocity components are given in dimensional form. Moreover, the same definitions for the Reynolds and the Deborah numbers are employed, namely

$$Re = \frac{2h\rho\langle v\rangle}{\eta_0}$$

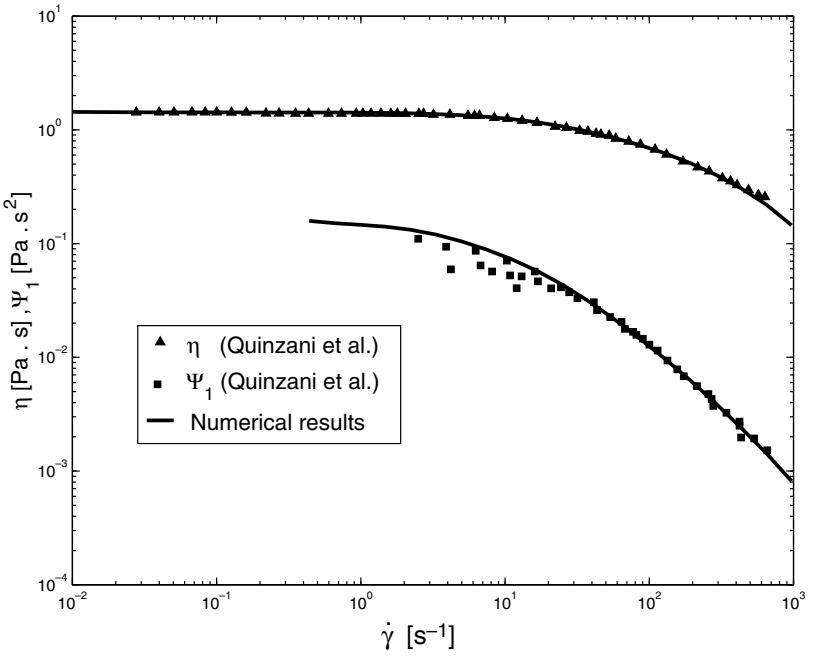

Fig. 13. Numerical results obtained for $\eta = \frac{\tau^{xy}}{\dot{\gamma}}$ and $\Psi_1 = \frac{\tau^{xx}-\tau^{yy}}{\dot{\gamma}^2}$ varying with $\dot{\gamma}$. Comparison with the experimental data presented by Quinzani et al. [38]. Input data used from Table 1.

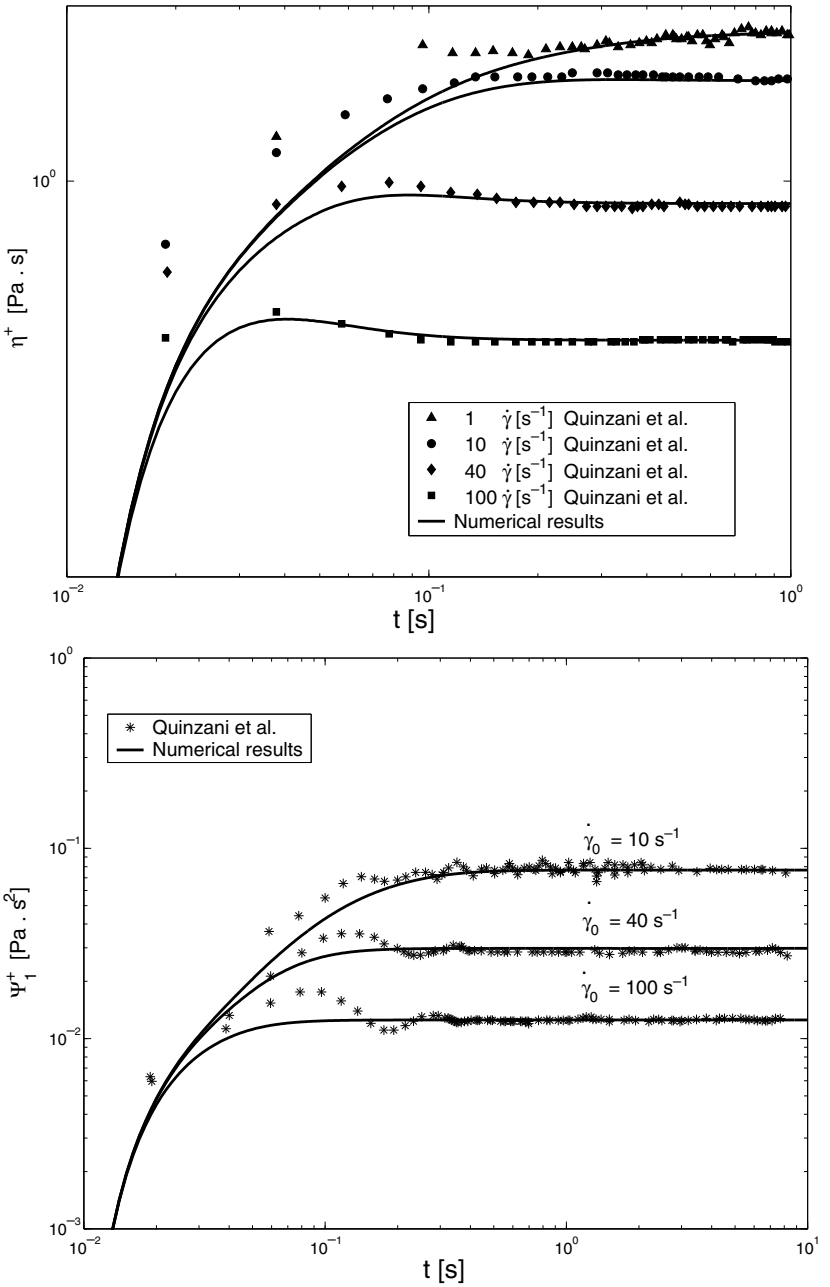

Fig. 14. Numerical results obtained for $\eta^+(t,\dot{\gamma}) = \frac{\tau^{xy}(t)}{\dot{\gamma}}$ and $\Psi_1^+(t,\dot{\gamma}) = \frac{\tau^{xx}(t)-\tau^{yy}(t)}{\dot{\gamma}^2}$ varying with time t. Comparison with the experimental data presented by Quinzani et al. [38]. Input data used from Table 1.

and

$$De = \lambda_0 \dot{\gamma},$$

where $\dot{\gamma} = \frac{\langle v \rangle}{h}$ and $\langle v \rangle$ is the bulk velocity at the downstream channel.

Quinzani et al. [37] performed measurements of the stress and velocity fields at six different flow rates. The predictions presented here use the model of Table 1 and are compared to the data of experiments 3 and 5 of Quinzani et al. [37], for which $Re = 0.27$ and $De = 1.39$ and $Re = 0.56$ and $De = 2.9$, respectively. The bulk velocities in the downstream channel were $\langle v \rangle = 7.44\,\mathrm{cm/s}$ and $\langle v \rangle = 15.5\,\mathrm{cm/s}$ for experiments 3 and 5, respectively. At the entrance (inflow) a Poiseuille velocity profile was imposed.

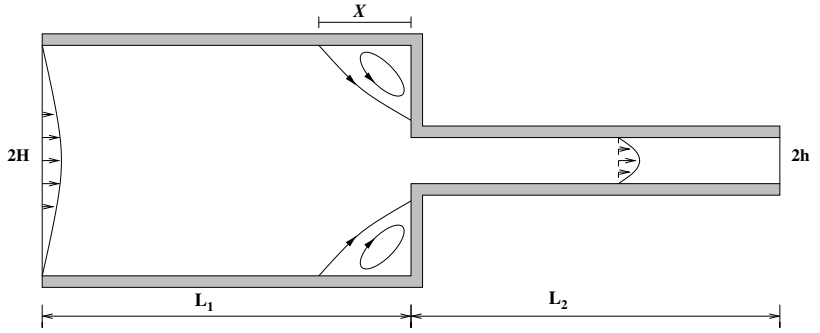

Fig. 15. Computational domain used in the simulation of the flow through a two-dimensional 4:1 contraction.

The comparison between the predictions and the experiments for $Re = 0.56$ and $De = 2.9$ are displayed in Figs. 16–18.

Figs. 16 and 17 show transverse and axial profiles of the streamwise velocity component (u) upstream the contraction plane, respectively. It can be observed the flow acceleration in the central region of the channel and the flow deceleration near the walls, as the fluid approaches the contraction plane. The agreement with the experimental data is better at points far from the contraction entrance. For the axial profiles, shown in Fig. 17, the agreement is better than for the transverse profiles, a fact also reported by Azaiez et al. [4].

Regarding the flow in the downstream channel, transverse profiles of u, N_1 and τ^{xy} are presented in Figs. 18–20 at different streamwise locations. The predicted profiles of τ^{xy} agree well with the experimental data of Quinzani et al. [37] whereas the predictions of u and N_1 agree with Quinzani's data only qualitatively. Nevertheless, the predictions of N_1 are fair and capture the smooth change in the shape from concave to convex and the quick variations near the centre plane. For the velocities, the predictions are higher in the central region of the channel and lower elsewhere suggesting that flow development is faster in the predictions than in the measurements.

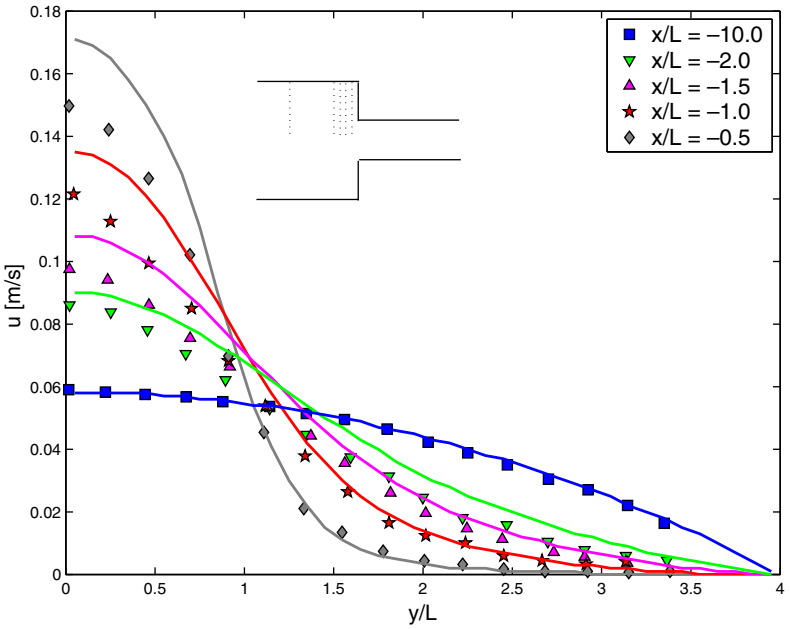

Fig. 16. Numerical simulation of the flow through a 4:1 contraction and comparison with experimental data of Quinzani et al. [37] ($Re = 0.56$ and $De = 2.9$). Numerical and experimental results obtained for the velocity $u(y)$ at various axial locations, x/L. Numerical solutions are represented by continuous curves.

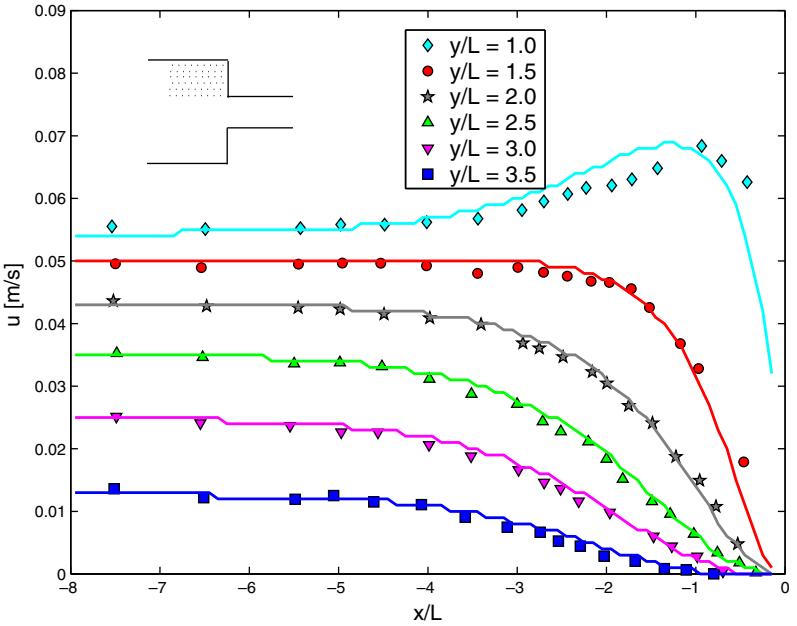

Fig. 17. Numerical simulation of the flow through a 4:1 contraction and comparison with experimental data of Quinzani et al. [37] ($Re = 0.56$ and $De = 2.9$). Numerical and experimental results obtained for the velocity $u(x)$ at various transverse locations, y/L. Numerical solutions are represented by continuous curves.

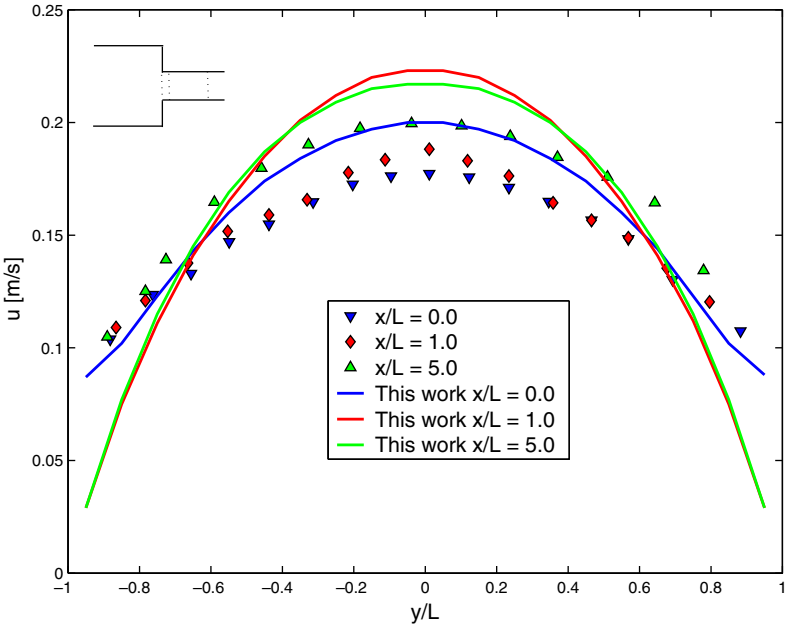

Fig. 18. Numerical simulation of the flow through a 4:1 contraction and comparison with experimental data of Quinzani et al. [37] ($Re = 0.56$ and $De = 2.9$). Numerical and experimental results obtained for the velocity component $u(y)$ at several axial locations, x/L along the exit channel. Numerical solutions are represented by continuous curves.

In general, the predictions far from the contraction entrance, where extensional flow is weak, are better than in this region because the constitutive equation was fitted only to shear rheology. The absence of extensional rheology data in Quinzani's paper does not allow us to be sure that the K–BKZ model is the

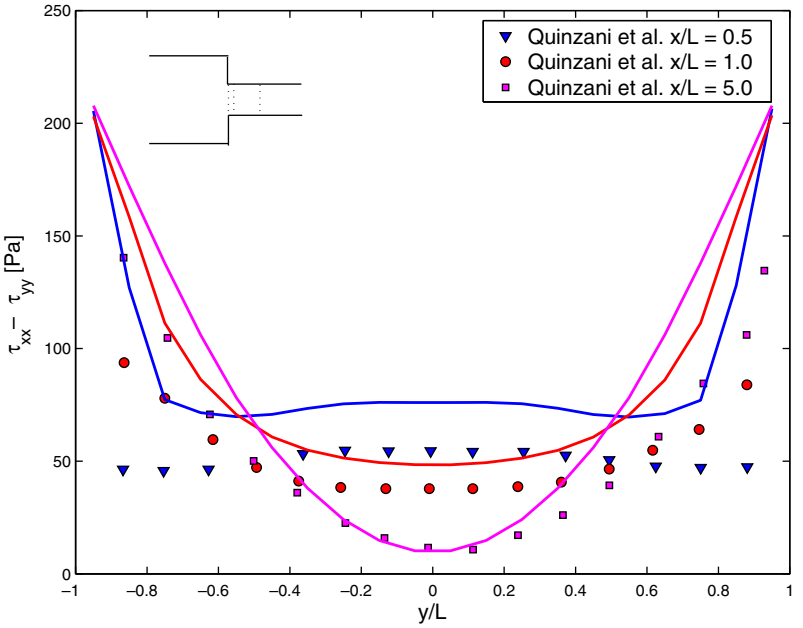

Fig. 19. Numerical simulation of the flow through a 4:1 contraction and comparison with experimental data of Quinzani et al. [37] ($Re = 0.56$ and $De = 2.9$). Numerical and experimental results obtained for $N_1(y)$ at several axial locations, x/L along the exit channel. Numerical solutions are represented by continuous curves.

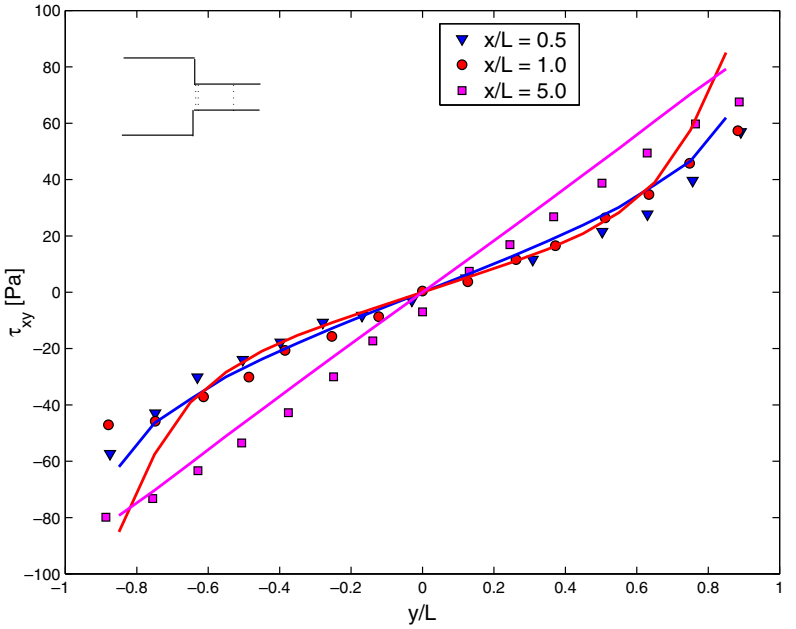

Fig. 20. Numerical simulation of the flow through a 4:1 contraction and comparison with experimental data of Quinzani et al. [37] ($Re = 0.56$ and $De = 2.9$). Numerical and experimental results obtained for $\tau^{xy}(y)$ at several axial locations, x/L along the exit channel. Numerical solutions are represented by continuous curves.

constitutive equation that better represents the behaviour of the fluid in flows with strong extensional effects. This is a problem that also affects other attempts of validation as will be shown next.

The profiles of the centreline velocity and N_1 along the centreline are plotted in Fig. 21 and compared with both the experimental data of Quinzani et al. [37] and the predictions of Azaiez et al. [4] using a differential

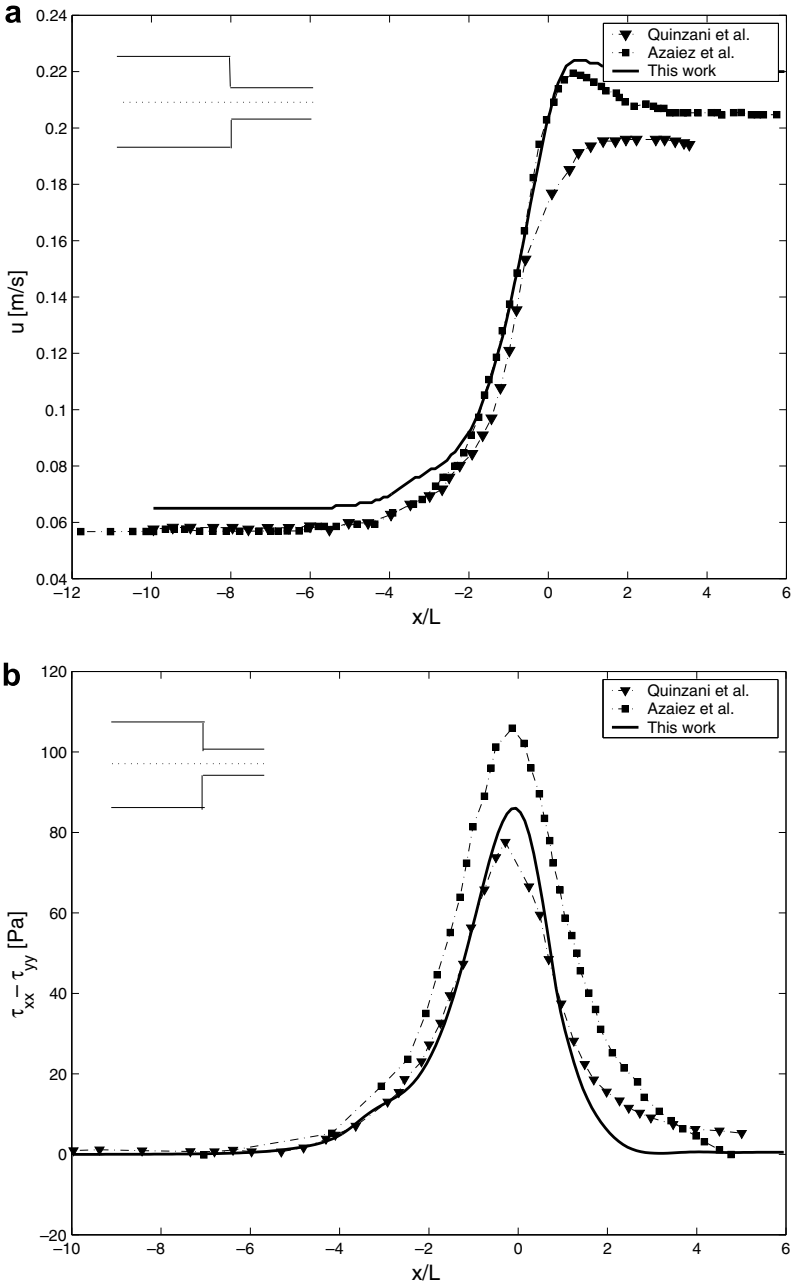

Fig. 21. Numerical simulation of the flow through a 4:1 contraction and comparison with experimental data of Quinzani et al. [37] ($Re = 0.56$ and $De = 2.9$). Comparison of experimental and numerical results along the centreline for (a) velocity component u and (b) first normal stress difference, N_1.

Giesekus model. Note that Azaiez et al. [4] also calculated Quinzani's flow using the PTT and FENE-P models and showed these predictions to be worse than their predictions using the Giesekus model. The agreement between the three sets of data in Fig. 21 is fair and whereas our predictions of u agree better with those of Azaiez et al. than with the experimental data, for N_1 it is the other way around. The level of agreement between our predictions and the measurements is similar to the level of agreement of Azaiez's predictions and Quinzani's experiments. We see that our and Azaiez's predictions are closer to each other than to the

experimental data, and this suggests that the discrepancies are associated with an inability of both constitutive equations (K–BKZ and Giesekus) to predict well the experimental data in extensional flow.

The comparison between the predictions and the experimental data for $Re = 0.27$ and $De = 1.39$ shows a similar behaviour as the case just presented ($Re = 0.56$ and $De = 2.9$), and the same level of agreement/disagreement, hence no further results are presented for conciseness.

8. Numerical simulation of contraction flows

In this section, results of numerical simulations of the flow through a planar 4:1 contraction, using the integral constitutive UCM and K–BKZ models, are presented. The flow domain is that shown in Fig. 15 and here the case of non-negligible inertia is investigated in detail, assessing the combined effects of viscoelasticity and inertia by varying the Weissenberg number for two different values of the Reynolds number ($Re = 0.1$ and $Re = 1.0$).

8.1. Single mode UCM model

For the single mode UCM model the input data employed were:

- *Length of the channels*: $L_1 = 16$ cm and $L_2 = 16$ cm;
- *Width of the channels*: $2H = 8$ cm and $2h = 2$ cm;
- *Mesh definition*: $\delta x = \delta y = 0.1$ cm (mesh with (80×320)-cells with a total of 16,000 **F**-cells);
- *Poisson solver tolerance*: $EPS = 10^{-10}$ (EPS is defined as the L_∞ residual norm);
- *Density of the fluid*: $\rho = 1000$ kg m^{-3}; dynamic viscosity: $\eta_0 = 10$ Pa s;
- *Number of fields used*: $N = 50$ (or number of points used to discretize the time interval $[0, t]$).

The scale parameters used for the normalization were: $L = 0.01$ m, $\lambda_0 = \lambda_1$ (defined below), $U = 0.1$ m s^{-1} for $Re = \rho UL/\eta_0 = 0.1$ and $U = 1$ m s^{-1} for $Re = 1$. At the fluid entrance a parabolic profile for the velocity was imposed, with $V_{\max} = U/4$. For the UCM model, the value of λ_1 and so the value of a_1 ($a_1 = \eta_0/\lambda_1$) were calculated as a function of the Weissenberg number, $We = \lambda_1 U/L$.

The FreeFlow2D code simulated the 4:1 contraction problem for the Weissenberg numbers $We = 0$ (Newtonian), $0.25, 0.5, 1.0, \ldots, 4$ from the start up until the steady state was reached.

Figs. 22 and 23 display the streamline patterns as a function of We for $Re = 0.1$ and $Re = 1$, respectively, and Table 2 lists the dimensionless size of the corner vortex which is also plotted in Fig. 24 for a better visualization of the effects of Re and We. As for $Re = 0$ (cf. [1]), Figs. 22 and 23 show that the length of the corner vortex for the UCM fluid decreases with We at each Reynolds number, with inertia also reducing its size. Moreover, for $We = 4$, the streamlines indicate the appearance of a small lip vortex at the reentrant corner for both values of Re, although here the mesh is still rather coarse. This flow has been simulated by various research groups using differential constitutive models like Oldroyd-B, UCM, PTT and these results are in agreement with their data (at least qualitatively). The appearance of a lip vortex for creeping flows ($Re = 0$) has been reported by several authors, such as Grossi et al. [12], who used a finite difference method for the Oldroyd-B model at $Re = 0.01$ and in the finite-volume calculations of Alves et al. [1] for the same fluid. These authors used very fine meshes and high resolution schemes reporting the appearance of a small lip vortex for $De \geqslant 1$. However, for $Re = 1$ Grossi et al. [12] did not report any lip vortex in their calculations. By using a semi-Lagrangian technique, Phillips and Williams [35] simulated the same flow for $Re = 0$ and $Re = 1$ and while they showed a small lip vortex for $We = 2$ and $We = 2.5$ at $Re = 0$, no lip vortex was seen for inertial flows at $Re = 1$.

In summary, the results obtained in this work for $Re = 0.1$ agree qualitatively with those presented in the literature, but show a lip vortex at $We = 4$ for Reynolds numbers between 0.1 and 1. To investigate whether our observation was due to insufficient mesh refinement, a simulation was carried out using a finer mesh having twice as many cells in each direction ((160×640)-cells) and the corresponding streamline plot at $We = 4$ is shown in Fig. 25. Again, the lip vortex is present, but now it is better resolved. This fact has not been previously reported in the literature at such high Weissenberg numbers and requires further investigation. Another

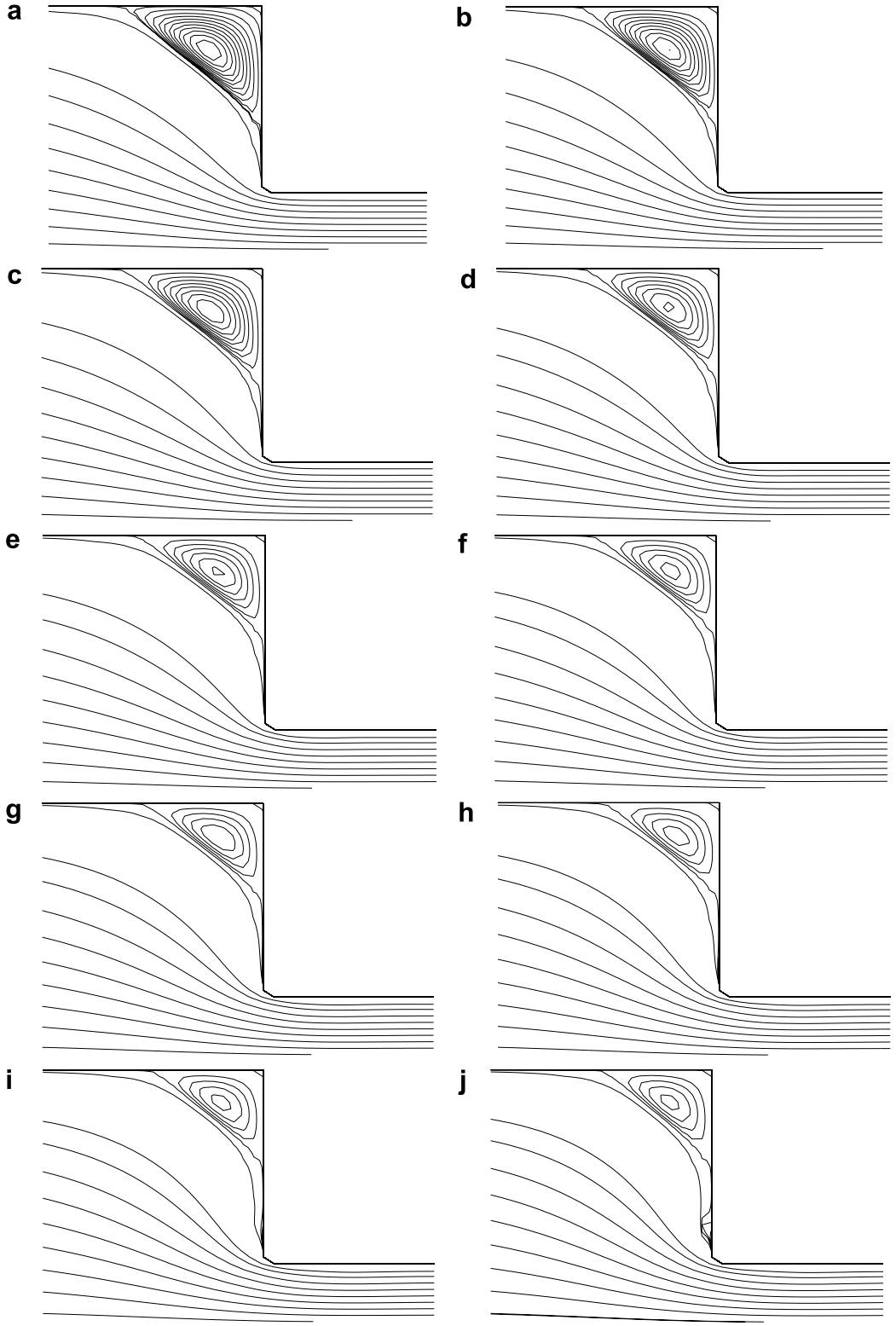

Fig. 22. Numerical simulation of the flow through a planar 4:1 contraction. Streamline plots obtained at $Re = 0.1$. (a) $We = 0$, (b) $We = 0.25$, (c) $We = 0.50$, (d) $We = 1.0$, (e) $We = 1.5$, (f) $We = 2.0$, (g) $We = 2.5$, (h) $We = 3.0$, (i) $We = 3.5$, (j) $We = 4.0$.

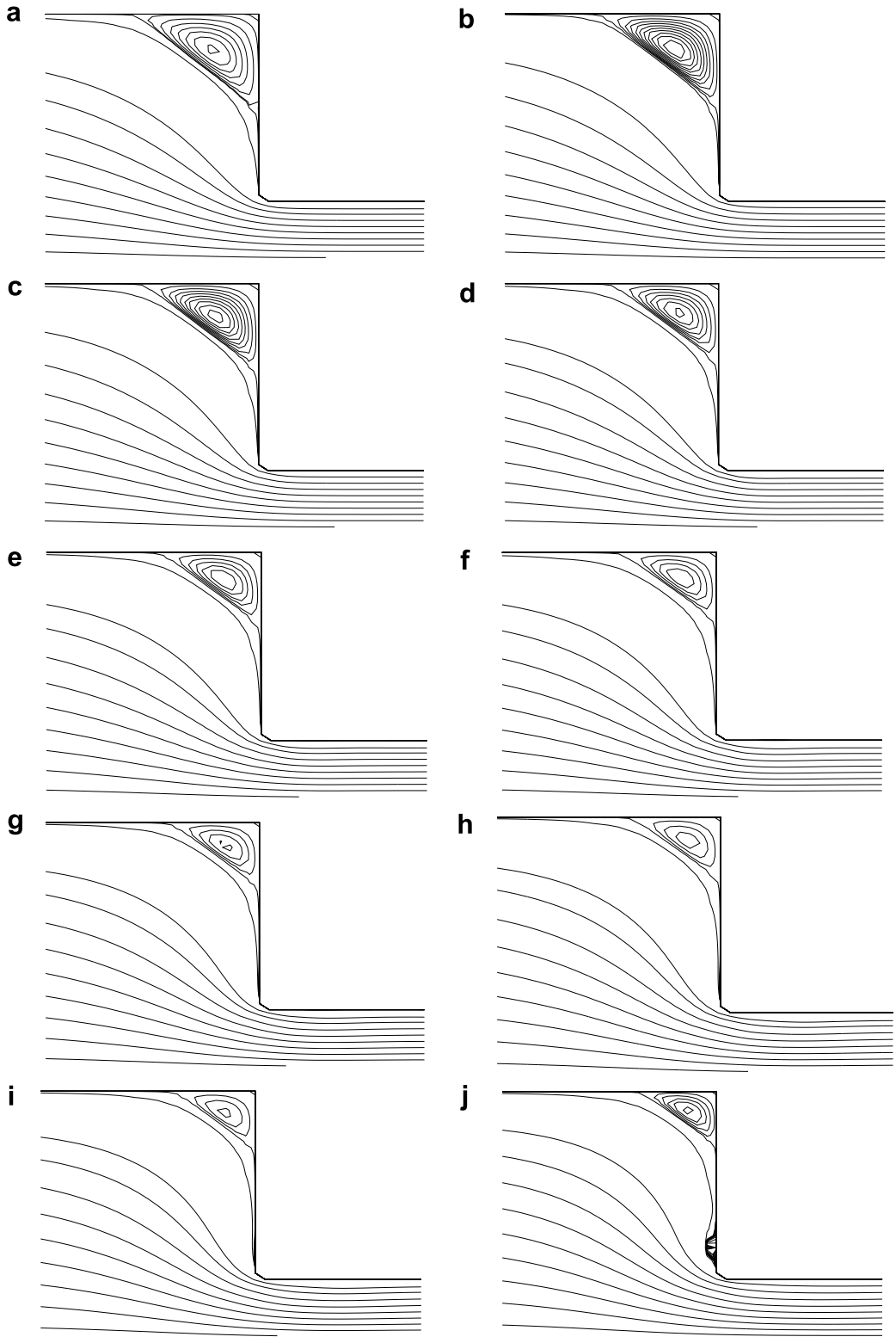

Fig. 23. Numerical simulation of the flow through a planar 4:1 contraction. Streamline plots obtained at $Re = 1.0$. (a) $We = 0$, (b) $We = 0.25$, (c) $We = 0.50$, (d) $We = 1.0$, (e) $We = 1.5$, (f) $We = 2.0$, (g) $We = 2.5$, (h) $We = 3.0$, (i) $We = 3.5$, (j) $We = 4.0$.

Table 2
Corner vortex size as a function of the Weissenberg number for the UCM model for $Re = 0.1$ and 1

We	0.0	0.25	0.5	1.0	1.5	2.0	2.5	3.0	3.5	4.0
$Re = 0.1$	1.447	1.417	1.376	1.304	1.246	1.202	1.165	1.133	1.111	1.095
$Re = 1.0$	1.271	1.227	1.176	1.089	1.016	0.959	0.909	0.856	0.820	0.768

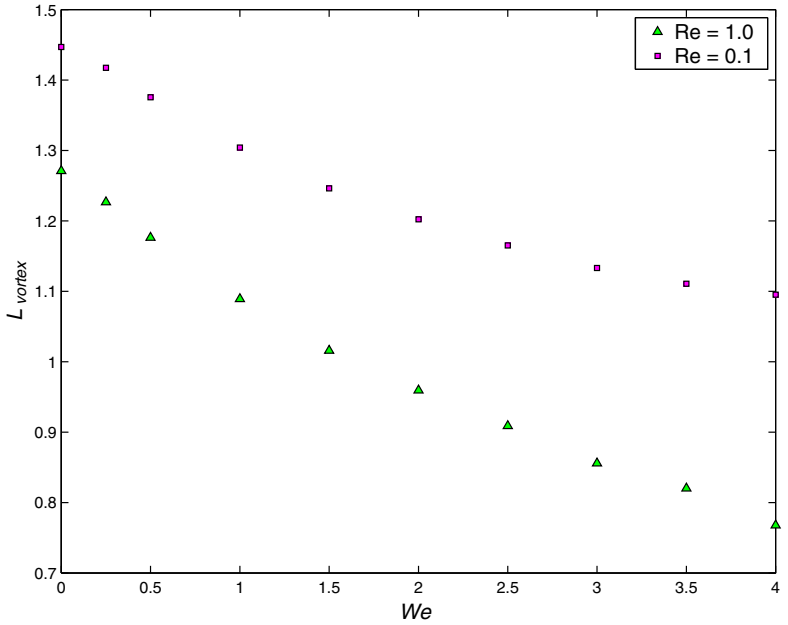

Fig. 24. Corner vortex size as a function of the Weissenberg number for the UCM model at $Re = 0.1$ and 1.

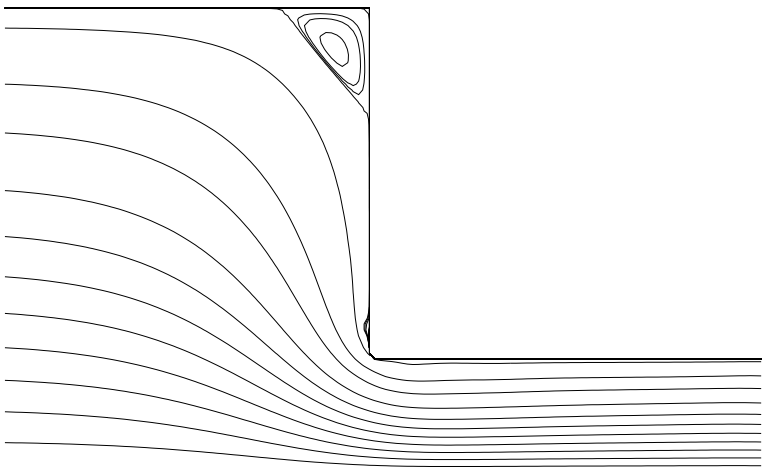

Fig. 25. Numerical simulation of the flow through a planar 4:1 contraction using the UCM model. Streamlines plots obtained at $Re = 1.0$ and $We = 4$ on a finer mesh with (160×640)-cells.

important conclusion here is that the present numerical method was able to calculate flows governed by the UCM model for the benchmark case of the 4:1 planar contraction, reaching high *We* numbers.

In order to further clarify these observations and to ensure that they are independent of the numerical method used, the finite-volume numerical method (FVM) of Alves et al. [1] was employed to simulate the same

flow for the UCM fluid at $Re = 0.1$ and 1 and the corresponding results compared with the predictions of the FreeFlow2D code. Here, only data for $Re = 1$ is shown for compactness. Note that these calculations using the FVM concern the UCM model described by a differential constitutive equation.

The finite-volume predictions were obtained using meshes **M2** and **M4** of Alves et al. [1], the characteristics of which are summarized in Table 3. The meshes used here with integral methods are uniform and consequently can only be refined near the contraction, at the cost of a large increase in the total number of cells, whereas the finite-volume code allows for meshes with cells of variable size. The consequence is that these meshes are significantly finer than those used here with the integral methods in the contraction region ($\Delta x^*_{\min} = \Delta y^*_{\min} = 0.1$), although mesh **M2** has less computational cells (10,587 against 16,000).

Mesh refinement is required especially near the contraction and to see this Fig. 26 compares the streamwise profile of the first normal stress difference, along the centreplane, obtained by the finite-volume code with the two meshes. This quantity is plotted in normalized form as N_1/τ_w, where τ_w is the fully-developed wall shear stress in the downstream channel. The first normal stress difference exhibits a peak around the contraction plane, which increases with fluid elasticity, and Fig. 26 shows that the results obtained with meshes **M2** and **M4** collapse, except for $We = 4$ where a small difference is seen, and that an increase of flow elasticity pushes the location of the peak downstream.

The corner vortex length plot of Fig. 27 compares the results obtained by the different methods and meshes. The extrapolated results presented in Fig. 27 were obtained using Richardson's extrapolation to the limit, and assuming that the FVM is second-order accurate, a result which has been demonstrated previously (e.g. [1]).

Table 3
Main characteristics of the meshes used in the finite-volume computations

Mesh	NC	$\Delta x^*_{\min} = \Delta y^*_{\min}$
M2	10,587	0.014
M4	42,348	0.0071

NC – Total number of cells; Δx^* – normalised cell size in streamwise direction ($\Delta x^* = \Delta x/h$); Δy^* – normalised cell size in transverse direction ($\Delta y* = \Delta y/h$).

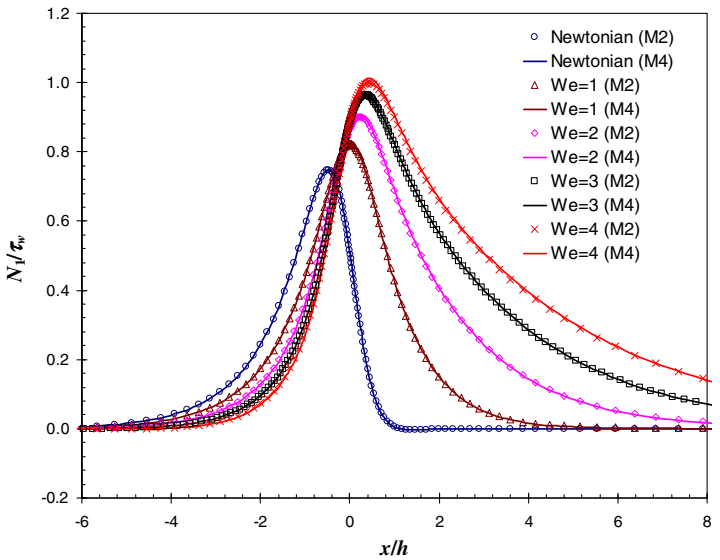

Fig. 26. Numerical simulation of the flow through a 4:1 planar contraction using the differential form of the UCM model, using the finite-volume code of Alves et al. [1] and meshes **M2** and **M4**. Contours of N_1/τ_w along the centreplane for $Re = 1$ and various Weissenberg numbers. Symbols: Mesh **M2**; lines: Mesh **M4**.

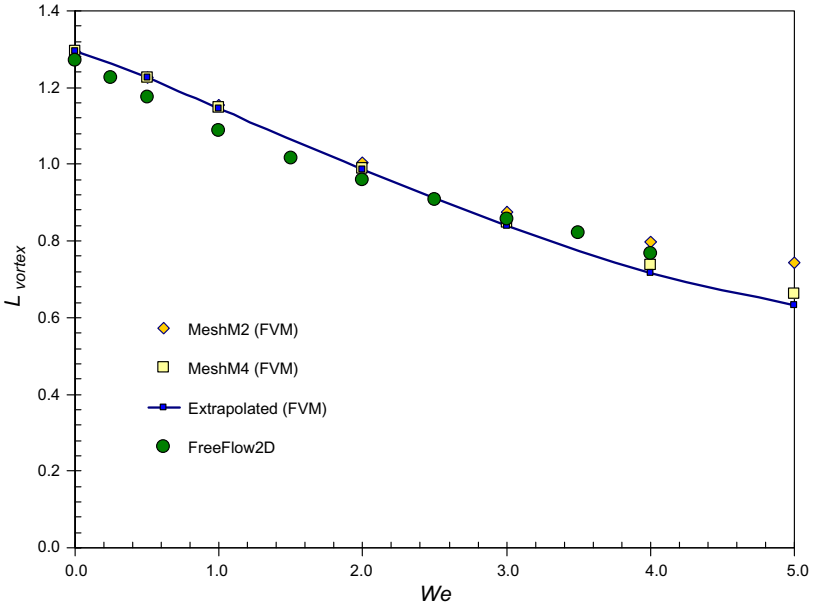

Fig. 27. Numerical simulation of the flow through a 4:1 planar contraction for $Re = 1$. Corner vortex length as a function of the Weissenberg number. Comparison with the finite-volume predictions obtained with the finite-volume code of [1].

The average difference between the FreeFlow2D results and the extrapolated FVM results is only 3.8%, showing the good accuracy of the FreeFlow2D results even though the rather coarseness of the mesh in the vicinity of the reentrant corner. We note that for the similar benchmark flow problem, at creeping flow conditions, the differences observed between the benchmark data of Alves et al. [1] and other results from literature is much higher, as can be assessed from Fig. 1 of Alves et al. [1]. More recently the accuracy of the benchmark data of [1] has been confirmed by Belblidia et al. [11].

The streamline contour plots presented in Fig. 28, for $We = 0$ and 4 at $Re = 1$, confirm the effect of We in reducing the size of the corner vortex and the existence at $We = 4$ of a small lip vortex, which here is well resolved by several cells due to the local mesh refinement. This lip vortex is accompanied by large viscoelastic normal stresses as is obvious from the comparison of the contour plots of N_1/τ_w in Fig. 29 for the Newtonian and $We = 4$ flows.

Still, there are small discrepancies between the predictions obtained by the finite difference method for the integral UCM equation and the finite-volume method for the differential UCM model, which can be seen in the comparisons of Figs. 30 and 31. These differences are due to insufficient mesh refinement close to the contraction in the FreeFlow2D calculations, the need of which increases as the Weissenberg number is raised. In Fig. 30, the plots of N_1/τ_w show that the FreeFlow2D code slightly overestimates this quantity, with the discrepancies increasing with We in both value and width of the peak, which widens and is located further downstream in the FreeFlow2D code results. On moving downstream a delay in flow redevelopment is also apparent with the FreeFlow2D code results, which again overpredicts N_1/τ_w. The larger peak values of N_1/τ_w obtained with the FreeFlow2D code are a consequence of a larger overshoot of the streamwise velocity along the centreplane, as can be seen in the plots of Fig. 31. Further downstream good agreement on N_1 is observed. We have further refined the mesh used in the FreeFlow2D simulations by increasing the number of cells in each direction by a factor of 1/3 and there have been improvements, as we can see from the velocity profiles in Fig. 32, in particular for the lower value of We. Unfortunately, the computational overhead of these calculations is enormous and this calculation took now circa 6 weeks of CPU time on a Sunworkstation 8 GB memory to converge. Clearly, further mesh refinement is required for an improved comparison, but the cost is prohibitive with our current available computational resources using the integral constitutive equation and the FreeFlow2D code.

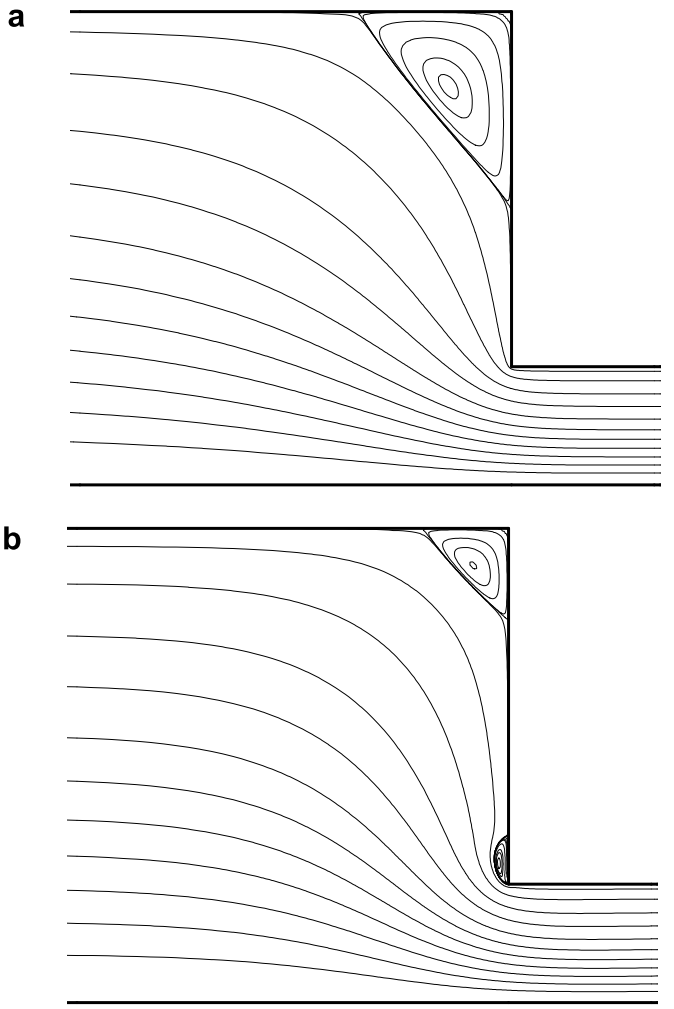

Fig. 28. Predicted streamlines for the flow through a 4:1 planar contraction for $Re = 1$ using the finite-volume code of Alves et al. [1]. (a) Newtonian; (b) UCM model with $We = 4$.

8.2. K–BKZ model

The flow through the 4:1 planar contraction was also simulated with the K–BKZ constitutive equation, but with different viscoelastic spectra than that used in Section 7.3.

The parameters used to specify the fluid rheology were the same used by Mitsoulis [25], who simulated the flow of fluid S1 through an axisymmetric 24:1 contraction, and are listed in Table 4. The scaling parameters used were $U = \langle v \rangle$ where $\langle v \rangle$ represents the average velocity in the exit channel, $L = h$ (see Fig. 15) and $\lambda_{\text{ref}} = \lambda_0$, where λ_0 is the relaxation time found for the UCM Maxwell (see [25]). Thus, the Weissenberg number is given by

$$We = \lambda_0 \frac{\langle v \rangle}{h} \tag{51}$$

with $\lambda_0 = 2.3$ s.

The computational domain was identical to that used for the UCM calculations.

The simulations for $We = 1$ and $We = 2$ were performed until $t = 20$ s and the remaining simulations ($We = 3, 4, 5, 6$) were carried out until time $t = 46$ s. The size of the corner vortex and the values of the corresponding Weissenberg and Reynolds numbers are listed in Table 5 and plots of the streamlines for

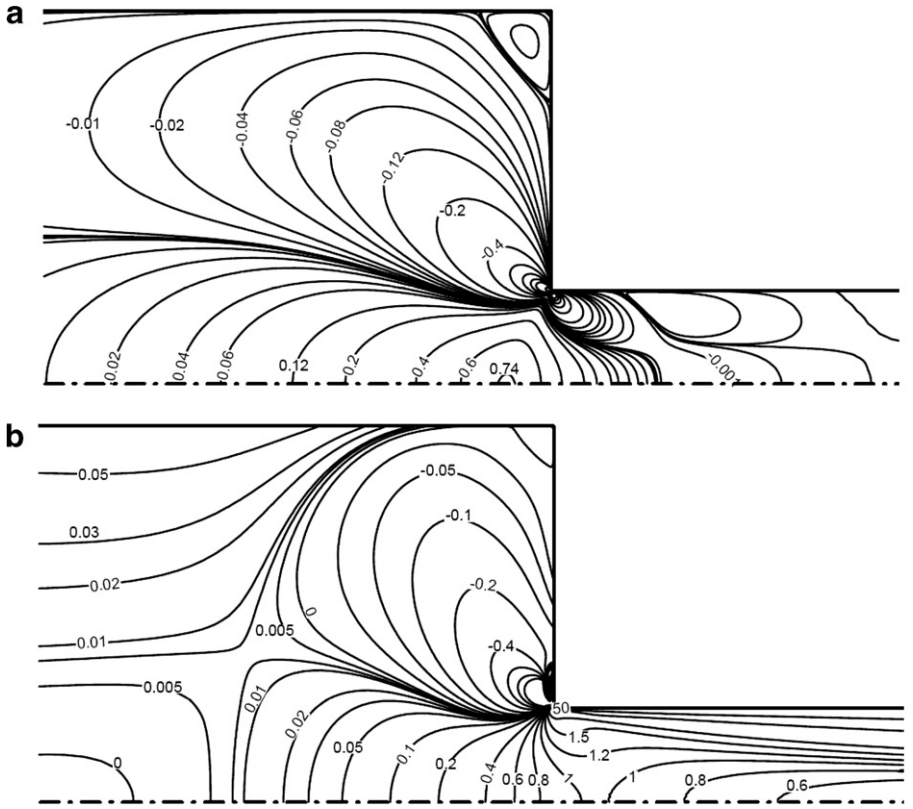

Fig. 29. Contours of N_1/τ_w for the flow through a 4:1 planar contraction at $Re = 1$ using the finite-volume code of Alves et al. [1]. (a) Newtonian; (b) UCM model with $We = 4$.

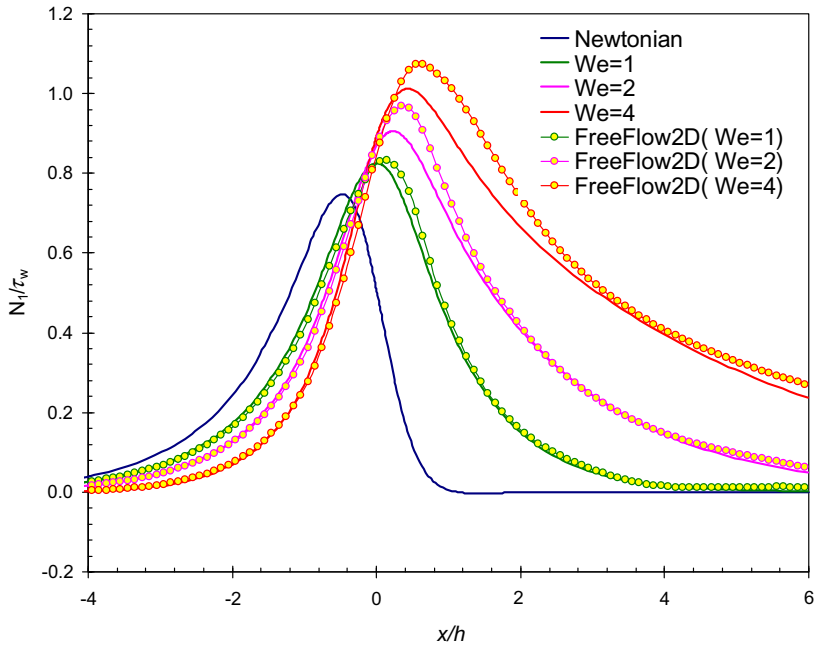

Fig. 30. Numerical simulation of the flow through a 4:1 planar contraction for $Re = 1$. Contours of N_1/τ_w along the centreplane for various Weissenberg numbers. Comparison with the finite-volume predictions obtained with the finite-volume code of [1].

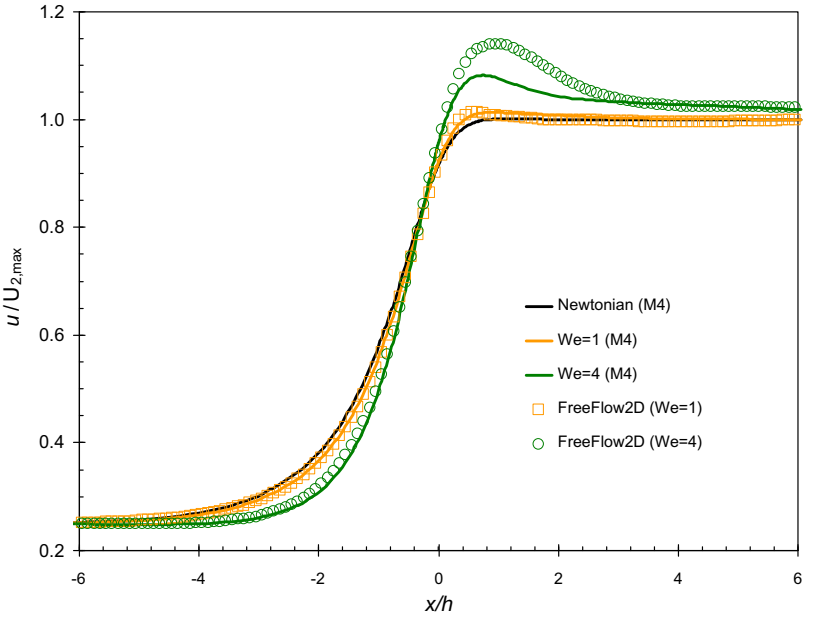

Fig. 31. Numerical simulation of the flow through a 4:1 planar contraction for $Re = 1$. Contours of the axial velocity in the centreplane near the contraction. Comparison with the finite-volume predictions obtained with the finite-volume code of [1].

$We = 1, 3, 5$ are shown in Fig. 33. As for the UCM model, the length of the corner vortex decreases with the Weissenberg number, but note that the Reynolds number is increasing at the same time so it is not easy to compare these values with those from the UCM model. The main conclusion here is that the present numerical method is able to simulate the flow of a multimode K–BKZ constitutive equation. Together with the simulations for the UCM model, this demonstrates the ability of the present numerical method to handle properly integral constitutive equations.

9. Conclusions

This work presented a numerical technique for simulating incompressible flows governed by the integral constitutive equations K–BKZ and upper-convected Maxwell (UCM). The technique developed in this work is based on the Marker-and-Cell method and employs finite differences on a staggered grid. The momentum and the mass conservation equations were solved by the GENSMAC methodology [47], while the constitutive equations were solved using the deformation fields method introduced by Peters et al. [34]. However, in this work the deformation fields method was improved in several ways: the Finger tensor is computed by a second-order interpolation formula and the integral constitutive equations were solved using a second-order quadrature scheme derived using the method of undetermined coefficients (see [16]). Validation results for both the UCM and K–BKZ models were presented. In addition, the flow through a planar 4:1 contraction was simulated and the numerical results obtained with the K–BKZ equation were compared with the experimental results of Quinzani et al. [37]. The results obtained with the UCM model were compared with the numerical results obtained by the finite-volume methodology of Alves et al. [2]. The single mode UCM fluid flow simulations were carried out at $Re = 0.1$ and 1 for We between 0 and 4 and it was found that the lip vortex previously predicted under creeping flow conditions is still present at higher Reynolds numbers. In summary, the numerical technique presented in this work proved to be able to simulate incompressible flows governed by the integral form of the K–BKZ and UCM models. Moreover, the technique presented in this paper can be easily extended to three-dimensional problems.

One important feature of this work was the use of the finite difference method for the simulation of incompressible inertial flows ($Re > 0$) described by integral equations. As far as the authors are aware the existing

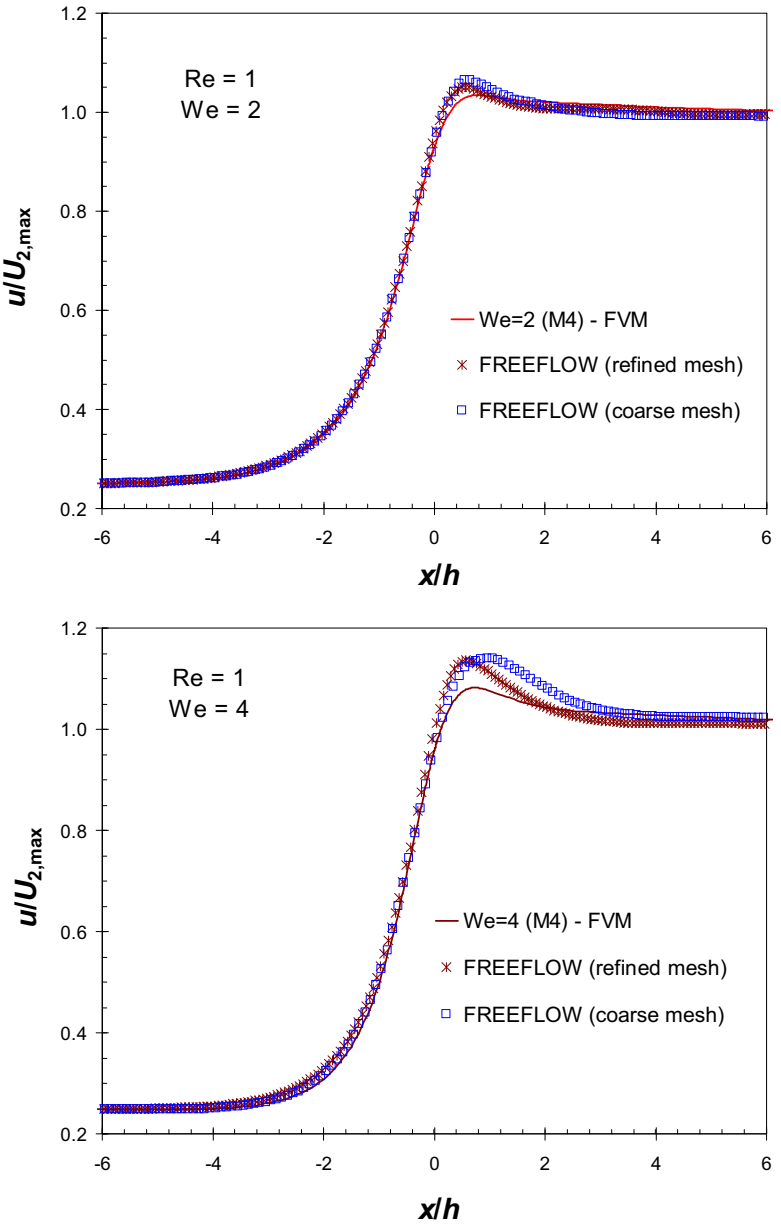

Fig. 32. Velocity profile at the symmetry axis using coarse mesh ($\delta x = \delta y = 0.1$ cm) and refined mesh ($\delta x = \delta y = 0.0667$ cm).

Table 4
Parameters used in the K–BKZ equation of a fluid S1 (see [25])

k	λ_k (s)	a_k (Pa)
1	0.0078	129.49
2	0.116	27.93
3	0.705	7.177
4	6.48	0.65

$\alpha = 25.0$, $\beta = 0.0011$, $\rho = 886$ kg m^{-3}, $\eta_0 = 13.68$ Pa s, $\lambda_0 = 2.3$ s.

Table 5
Corner vortex size obtained with the K–BKZ model for various values of *We* and *Re*

(We, Re)	$(1.0, 0.280)$	$(2.0, 0.560)$	$(3.0, 0.845)$	$(4.0, 1.130)$	$(5.0, 1.410)$	$(6.0, 1.690)$
L_{vortex}	1.351	1.095	1.020	0.920	0.867	0.701

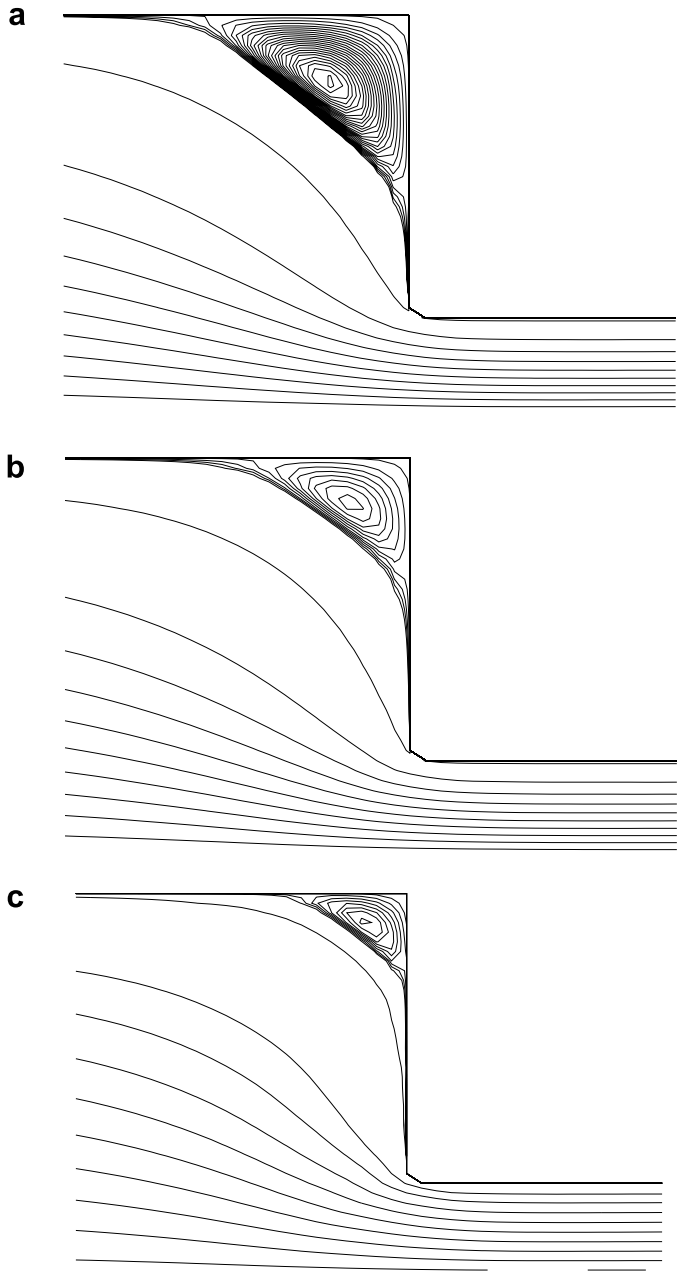

Fig. 33. Numerical simulation of the flow through a planar 4:1 contraction using the K–BKZ constitutive equation for various Weissenberg and Reynolds numbers. (a) $We = 1, Re = 0.280$; (b) $We = 3, Re = 0.845$; (c) $We = 6, Re = 1.690$.

techniques for solving integral constitutive equations have employed the finite element method to solve incompressible creeping flows $(Re = 0)$ only.

Acknowledgements

The first author thanks the support of the Brazilian funding agency CNPq (Research Grant Nos. 474040/2003-8, 523141/94) and CAPES pos-doc Grant No. 0121/07-0. The authors also acknowledge support from CAPES (Proposal CAPES/GRICES Grant No. 136/5) and FAPESP (Research Grant No. 2004/16064-9). Funding from GRICES (Portugal) is also acknowledged.

References

[1] M.A. Alves, P.J. Oliveira, F.T. Pinho, Benchmark solutions for the flow of Oldroyd-b and PTT fluids in planar contractions, J. Non-Newtonian Fluid Mech. 110 (2003) 45–75.
[2] M.A. Alves, P.J. Oliveira, F.T. Pinho, A convergent and universally bounded interpolation scheme for treatment of advection, Int. J. Numer. Methods Fluids 41 (2003) 47–75.
[3] M.A. Alves, F.T. Pinho, P.J. Oliveira, Visualization of Boger fluid flows in a 4:1 square–square contraction, AIChE J. 51 (2005) 2908–2922.
[4] J. Azaiez, R. Guénette, A. A-Kadi, Numerical simulation of viscoelastic flows through a planar contraction, J. Non-Newtonian Fluid Mech. 62 (1996) 253–277.
[5] B. Bernstein, E.A. Kearsley, L.J. Zapas, A study of stress relaxation with finite strain, Trans. Soc. Rheol. VII (1963) 391–410.
[6] R.B. Bird, R.C. Armstrong, O. Hassager, Dynamics of Polymeric Liquids, vol. 1, John Wiley & Sons, 1987.
[7] B. Caswell, M. Viriyayuthakorn, Finite element simulation of die swell for a Maxwell fluid, J. Non-Newtonian Fluid Mech. 12 (1983) 13–29.
[8] A.B. Costacurta, Estratégias "upwind" e modelagem k-epsilon para simulação numérica de escoamentos com superfícies livres em altos números de Reynolds, MSc Thesis, ICMC/USP, São Carlos, Brazil, 2005.
[9] R. Evans, K. Walters, Flow characteristics associated with abrupt changes in geometry in the case of highly elastic liquids, J. Non-Newtonian Fluid Mech. 20 (1986) 11–29.
[10] R. Evans, K. Walters, Further remarks on the lip-vortex mechanism of vortex enhancement in planar-contraction flows, J. Non-Newtonian Fluid Mech. 32 (1989) 95–105.
[11] B.P.F. Belblidia, H. Matallah, M. Webster, Alternative subcell discretisations for viscoelastic flow. Part I: stress interpolation, J. Non-Newtonian Fluid Mech. 146 (2007) 59–78.
[12] L. Grossi, Desenvolvimento de métodos numéricos para a simulação de escoamentos não-newtonianos e viscoelásticos com superfícies livres, PhD thesis, ICMC-USP, São Carlos, Brazil, 2003.
[13] F.H. Harlow, J.E. Welch, The MAC method, Phys. Fluids 8 (1965) 2182–2189.
[14] O. Hassager, C. Bisgaard, A Lagrangian finite element method for the simulation of non-Newtonian liquids, J. Non-Newtonian Fluid Mech. 12 (1983) 153–164.
[15] M.A. Hulsen, E.A.J.F. Peters, B.H.A.A. van den Brule, A new approach to the deformation fields method for solving complex flows using integral constitutive equations, J. Non-Newtonian Fluid Mech. 98 (2001) 201–221.
[16] E. Isaacson, H.B. Keller, Analysis of Numerical Methods, Wiley, 1996.
[17] A. Kaye, Non-Newtonian Flow in Incompressible Fluids, College of Aeronautics, 1962.
[18] R. Keunings, Finite element method for integral viscoelastic fluids, Rheol. Rev. 1 (2003) 167–195.
[19] X.L. Luo, A control volume approach for integral viscoelastic models and its application to contraction flow of polymer melts, J. Non-Newtonian Fluid Mech. 64 (1996) 173–189.
[20] X.L. Luo, E. Mitsoulis, An efficient algorithm for strain history tracking in finite element computations of non-Newtonian fluids with integral constitutive equations, Int. J. Numer. Methods Fluids 11 (1990) 1015–1031.
[21] X.L. Luo, E. Mitsoulis, A numerical study of the effect of elongational viscosity on vortex growth in contraction flows of polyethylene, J. Rheol. 34 (1990) 309–342.
[22] X.L. Luo, R.I. Tanner, A streamline element scheme for solving viscoelastic flow problems. Part II: integral constitutive models, J. Non-Newtonian Fluid Mech. 22 (1986) 61–89.
[23] J. Marchal, M. Crochet, A new mixed finite element for calculating viscoelastic flow, J. Non-Newtonian Fluid Mech. 26 (1987) 77–114.
[24] E. Mitsoulis, Numerical simulation of planar entry flow for a polyisobutylene solution using an integral constitutive equation, J. Rheol. 37 (1993) 1029–1040.
[25] E. Mitsoulis, Further results for the entry flow of fluid S1, J. Non-Newtonian Fluid Mech. 97 (2001) 149–158.
[26] G. Mompean, M. Deville, Unsteady finite volume simulation of Oldroyd-B fluid through a three-dimensional planar contraction, J. Non-Newtonian Fluid Mech. 72 (1997) 253–279.
[27] V. Ngamaramvaranggul, M. Webster, Computation of free surface flows with a Taylor–Galerkin/pressure correction algorithm, Int. J. Numer. Methods Fluids 33 (2000) 993–1026.
[28] V. Ngamaramvaranggul, M. Webster, Simulation of coating flows with slip effects, Int. J. Numer. Methods Fluids 33 (2000) 961–992.
[29] M. Normandin, J.-R. Clermont, J. Guillet, C. Raveyene, Three-dimensional extrudate swell experimental and numerical studies of a polyethylene melt obeying a memory-integral equation, J. Non-Newtonian Fluid Mech. 87 (1999) 1–25.

[30] J. Oliveira, Desenvolvimento de um sistema de simulação de escoamentos de fluidos com superfícies livres bidimensionaiss, MSc Thesis, ICMC/USP, São Carlos, Brazil, 1999.
[31] P. Olley, P.D. Coates, An approximation to the K–BKZ constitutive equation, J. Non-Newtonian Fluid Mech. 69 (1997) 239–254.
[32] R.G. Owens, T.N. Phillips, Computational Rheology, Imperial College Press, 2002.
[33] A.C. Papanastasiou, L. Scriven, C. Macosko, An integral constitutive equation for mixed flows: viscoelastic characterization, J. Rheol. 27 (1983) 387–410.
[34] E.A.J.F. Peters, M.A. Hulsen, B.H.A.A. van den Brule, Instationary Eulerian viscoelastic flow simulation using time separable Rivlin–Sawyers constitutive equations, J. Non-Newtonian Fluid Mech. 89 (2000) 209–228.
[35] T. Phillips, A. Williams, Viscoelastic flow through a planar contraction using a semi-Lagrangian finite volume method, J. Non-Newtonian Fluid Mech. 87 (1999) 215–246.
[36] B. Purnode, M. Crochet, Flows of polymer solutions through contractions. Part 1: flows of polyacrylamide solutions through planar contractions, J. Non-Newtonian Fluid Mech. 65 (1996) 269–289.
[37] L.M. Quinzani, R.C. Armstrong, R.A. Brown, Birefringence and laser-Doppler velocimetry (LDV) studies of viscoelastic flow through a planar contraction, J. Non-Newtonian Fluid Mech. 52 (1994) l–36.
[38] L.M. Quinzani, G.H. McKinley, R.A. Brown, R.C. Armstrong, Modeling the rheology of polyisobutylene solutions, J. Rheol. 34 (1990) 705–748.
[39] D. Rajagopalan, R.C. Armstrong, R.A. Brown, Finite element methods for calculation of steady viscoelastic flow using constitutive equations with a Newtonian viscosity, J. Non-Newtonian Fluid Mech. 36 (1990) 159–192.
[40] H.K. Rasmussen, Lagrangian viscoelastic flow computations using the Rivlin–Sawyers constitutive model, J. Non-Newtonian Fluid Mech. 92 (2000) 227–243.
[41] H.K. Rasmussen, O. Hassager, Three-dimensional simulations of viscoelastic instability in polymeric filaments, J. Non-Newtonian Fluid Mech. 82 (1999) 189–202.
[42] R.I. Tanner, A theory of die-swell, J. Polym. Sci.: Part A-2 8 (1970) 2067–2078.
[43] R.I. Tanner, A new theory of extrudate swell, J. Non-Newtonian Fluid Mech. 6 (1980) 289–302.
[44] R.I. Tanner, From A to (BK)Z in constitutive relations, J. Rheol. 7 (1988) 673–702.
[45] M.F. Tomé, N. Mangiavacchi, J.A. Cuminato, A. Castelo, S. McKee, A finite difference technique for simulating unsteady viscoelastic free surface flows, J. Non-Newtonian Fluid Mech. 106 (2002) 61–106.
[46] M.F. Tomé, B. Duffy, S. McKee, A numerical technique for solving unsteady non-Newtonian free surface flows, J. Non-Newtonian Fluid Mech. 62 (1996) 9–34.
[47] M.F. Tomé, S. McKee, GENSMAC: a computational marker and cell method for free surface flows in general domains, J. Comput. Phys. 110 (1994) 171–186.
[48] D. Trebotich, P. Colella, G. Miller, A stable and convergent scheme for viscoelastic flow in contraction channels, J. Comput. Phys. 205 (2005) 315–342.
[49] H.M. Van Heel, M.A. Hulsen, B.H.A.A. Van den Brule, Numerical simulation of the Doi–Edwards model in complex flows, J. Rheol. 43 (1999) 1239–1260.
[50] M. Viriyayuthakorn, B. Caswell, Finite element simulation of viscoelastic flow, J. Non-Newtonian Fluid Mech. 6 (1980) 245–267.
[51] S.A. White, D.G. Baird, The importance of extensional flow properties on planar entry flow patterns of polymer melts, J. Non-Newtonian Fluid Mech. 20 (1986) 93–101.
[52] S. Xue, N. Phan-Thien, R.I. Tanner, Numerical study of secondary flows of viscoelastic fluid in straight pipes by an implicit finite volume method, J. Non-Newtonian Fluid Mech. 59 (1995) 191–213.
[53] S. Xue, N. Phan-Thien, R.I. Tanner, Three-dimensional numerical simulations of viscoelastic flows through planar contractions, J. Non-Newtonian Fluid Mech. 74 (1998) 195–245.